Micromorphic Crystal Plasticity

S. Forest, J. R. Mayeur, and D. L. McDowell

Contents

S. Forest (✉)
Centre des Matériaux UMR 7633, Mines ParisTech, CNRS, Evry Cedex, France
e-mail: samuel.forest@mines-paristech.fr

J. R. Mayeur
Theoretical Division, Los Alamos National Laboratory, Los Alamos, NM, USA
e-mail: jason.mayeur@gmail.com

D. L. McDowell
Woodruff School of Mechanical Engineering, School of Materials Science and Engineering,
Georgia Institute of Technology, Atlanta, GA, USA
e-mail: david.mcdowell@me.gatech.edu

1

Abstract

The micromorphic approach to crystal plasticity represents an extension of the micropolar (Cosserat) framework, which is presented in a separate chapter. Cosserat crystal plasticity is contained as a special constrained case in the same way as the Cosserat theory is a special restricted case of Eringen's micromorphic model, as explained also in a separate chapter. The micromorphic theory is presented along the lines of Aslan et al. (Int J Eng Sci 49:1311–1325, 2011) and Forest et al. (Micromorphic approach to crystal plasticity and phase transformation. In: Schroeder J, Hackl K (eds) Plasticity and beyond. CISM international centre for mechanical sciences, courses and lectures, vol 550, Springer, pp 131–198, 2014) and compared to the micropolar model in some applications. These extensions of conventional crystal plasticity aim at incorporating the dislocation density tensor introduced by Kröner (Initial studies of a plasticity theory based upon statistical mechanics. In: Kanninen M, Adler W, Rosenfield A, Jaffee R (eds) Inelastic behaviour of solids. McGraw-Hill, pp 137–147, 1969). and Cermelli and Gurtin (J Mech Phys Solids 49:1539–1568, 2001) into the constitutive framework. The concept of dislocation density tensor is equivalent to that of the so-called geometrically necessary dislocations (GND) introduced by Ashby (The deformation of plastically non-homogeneous alloys. In: Kelly A, Nicholson R (eds) Strengthening methods in crystals. Applied Science Publishers, London, pp 137–192, 1971). The applications presented in this chapter deal with pile-up formation in laminate microstructures and strain localization phenomena in polycrystals.

Introduction

The micromorphic approach to crystal plasticity represents an extension of the micropolar (Cosserat) framework which is presented in a separate chapter. Cosserat crystal plasticity is contained as a special constrained case in the same way as the Cosserat theory is a special restricted case of Eringen's micromorphic model, as explained also in a separate chapter. The micromorphic theory is presented along the lines of Aslan et al. (2011) and Forest et al. (2014) and compared to the micropolar model in some applications. These extensions of conventional crystal plasticity aim at incorporating the dislocation density tensor introduced by Kröner (1969) and Cermelli and Gurtin (2001) into the constitutive framework. The concept of dislocation density tensor is equivalent to that of so-called geometrically necessary dislocations (GND) introduced by Ashby (1971).

The links between the micromorphic continuum and the plasticity of crystalline materials have been recognized very early by Claus and Eringen (1969) and Eringen

and Claus ([1970]). Lattice directions in a single crystal can be regarded as directors that rotate and deform as they do in a micromorphic continuum. The fact that lattice directions can be rotated and stretched in a different way than material lines connecting individual atoms, especially in the presence of static or moving dislocations, illustrates the independence between directors and material lines in a micromorphic continuum, even though their deformation can be related at the constitutive level.

The objective of the present chapter is to formulate a finite deformation micromorphic extension of conventional crystal plasticity to account for GND effects in single crystals. It also provides analytical predictions of size effects on the yield strength and kinematic hardening of laminate microstructures made of an elastic layer and an elastic–plastic single-crystal layer undergoing single slip. The theory is called the *microcurl* model because the evaluation of the curl of the microdeformation, instead of its full gradient, is sufficient to account for the effect of the dislocation density tensor.

The models proposed in this section for single crystals fall in the class of anisotropic elastoviscoplastic micromorphic media for which constitutive frameworks at finite deformations have been proposed in Forest and Sievert ([2003]), Lee and Chen ([2003]), Grammenoudis and Tsakmakis ([2009]), Sansour et al. ([2010]), and Regueiro [2010]; see the corresponding chapter in this handbook. In fact, the micromorphic approach can be applied not only to the total deformation by introducing the microdeformation field but can also be restricted to plastic deformation, for specific application to size effects in plasticity, or to damage variables for application to regularized simulation of crack propagation, as proposed in Forest ([2009], [2016]) and Hirschberger and Steinmann ([2009]).

The outline of this chapter is as follows. The crystal plasticity model formulated within Eringen's micromorphic framework is presented at finite deformation in section "The Microcurl Model at Finite Deformation," together with its linearization. Size effects predicted by the model are illustrated in section "Size Effects in a Two-Phase Single-Crystal Laminate." Some constitutive laws involving the dislocation density tensor are discussed in section "Free Energy Potentials for Micromorphic Crystal Plasticity" with an application to cyclic plasticity in single crystals. Finally, the model is used to predict the response of polycrystalline metals and alloys in section "Grain Size Effects in Polycrystals."

The Microcurl Model at Finite Deformation

Model Formulation

Balance Equations

The degrees of freedom of the proposed theory are the displacement vector $\boldsymbol{u}$ and the microdeformation variable $\widehat{\boldsymbol{\chi}}^p$, a generally nonsymmetric second-rank tensor. The field $\widehat{\boldsymbol{\chi}}^p(\boldsymbol{X})$ is generally not compatible, meaning that it does not derive from a vector field. The exponent ^{p} indicates, in advance, that this variable will eventually

be constitutively related to plastic deformation occurring at the material point. In particular, the microdeformation $\widehat{\boldsymbol{\chi}}^{p}$ is treated as an invariant quantity with respect to rigid body motion. The polar decomposition of the microdeformation contains the polar rotation $\overline{\mathbf{R}}$ used in the micropolar crystal plasticity theory and a symmetric microstretch tensor. As a result, when this microstretch tensor is close to the identity tensor, the micromorphic model reduces to the micropolar one.

A first gradient theory is considered with respect to the degrees of freedom. However, the influence of the microdeformation gradient is limited to its curl part because of the intended relation to the dislocation density tensor associated with the curl of plastic distortion. The following sets of degrees of freedom and of their gradients are therefore defined:

$$DOF = \left\{\boldsymbol{u}, \quad \widehat{\boldsymbol{\chi}}^{p}\right\}, \ GRAD = \left\{\mathbf{F} := 1 + \boldsymbol{u} \otimes \nabla_0, \ \mathbf{K} := \text{Curl } \widehat{\boldsymbol{\chi}}^{p}\right\} \qquad (1)$$

The following definition of the curl operator is adopted:

$$\text{Curl } \widehat{\boldsymbol{\chi}}^{p} := \frac{\partial \widehat{\boldsymbol{\chi}}^{p}}{\partial X_k} \times \boldsymbol{e}_k, \ K_{ij} \ := \ \in_{jkl} \frac{\partial \widehat{\chi}^{p}_{ik}}{\partial X_l} \qquad (2)$$

where $\in_{ijk}$ is the permutation tensor.

The method of virtual power is used to derive the balance and boundary conditions, following Germain (1973). For that purpose, the power density of internal forces is defined as a linear form with respect to the velocity fields and their Eulerian gradients:

$$p^{(i)} = \boldsymbol{\sigma} \ : (\dot{\boldsymbol{u}} \otimes \nabla) + \mathbf{s} : \dot{\widehat{\boldsymbol{\chi}}}^{p} + \mathbf{M} : \text{curl } \dot{\widehat{\boldsymbol{\chi}}}^{p}, \ \forall \boldsymbol{x} \ \in \ V \qquad (3)$$

Here, the conjugate quantities are the Cauchy stress tensor $\boldsymbol{\sigma}$, which is symmetric for objectivity reasons; the microstress tensor, $\mathbf{s}$; and the generalized couple-stress tensor $\mathbf{M}$. The curl of the microdeformation rate is defined as:

$$\text{curl } \dot{\widehat{\boldsymbol{\chi}}}^{p} := \ \in_{jkl} \frac{\partial \dot{\widehat{\chi}}^{p}_{ik}}{\partial x_l} \ \boldsymbol{e}_i \otimes \boldsymbol{e}_j = \dot{\mathbf{K}} \ \mathbf{F}^{-1} \qquad (4)$$

The form of the power density of internal forces dictates the form of the power density of contact forces:

$$p^{(c)} = \boldsymbol{t} \cdot \dot{\boldsymbol{u}} + \mathbf{m} : \dot{\widehat{\boldsymbol{\chi}}}^{p}, \ \forall \boldsymbol{x} \ \in \ \partial V \qquad (5)$$

where $\boldsymbol{t}$ is the usual simple traction vector and $\mathbf{m}$ is the double-traction tensor. The principle of virtual power is stated in the static case and in the absence of volume forces for the sake of brevity:

$$-\int_{D} p^{(i)} \ dV + \int_{\partial D} p^{(c)} \ dS = 0 \qquad (6)$$

for all virtual fields $\dot{\boldsymbol{u}}, \dot{\widehat{\boldsymbol{\chi}}}^p$ and any subdomain $D \subset V$. By application of the Gauss divergence theorem, assuming sufficient regularity of the fields, this statement expands into:

$$\int_V \frac{\partial \sigma_{ij}}{\partial x_j} \ \dot{u}_i \ dV + \int_V \left(\in_{kjl} \frac{\partial M_{ik}}{\partial x_l} - s_{ij} \right) \ \dot{\widehat{\chi}}^p_{ij} \ dV$$
$$+ \int_{\partial V} \left(t_i - \sigma_{ij} n_j \right) \ \dot{u}_i \ dS + \int_{\partial V} \left(m_{ik} - \in_{jkl} M_{ij} n_l \right) \ \dot{\widehat{\chi}}^p_{ik} \ dS = 0, \quad \forall \dot{u}_i, \forall \dot{\widehat{\chi}}^p_{ij}$$

which leads to the two-field equations of balance of momentum and generalized balance of moment of momentum:

$$\text{div} \ \boldsymbol{\sigma} = 0, \ \text{curl} \ \mathbf{M} + \mathbf{s} = 0, \ \forall \boldsymbol{x} \in V \tag{7}$$

and two boundary conditions:

$$\boldsymbol{t} = \boldsymbol{\sigma} \cdot \boldsymbol{n}, \ \mathbf{m} = \mathbf{M} \cdot \boldsymbol{\in} \cdot \boldsymbol{n}, \ \forall \boldsymbol{x} \in \partial V \tag{8}$$

the index representation of the latter relation being $m_{ij} = M_{ik} \in_{kjl} n_l$. These balance equations can be compared to the corresponding ones in the chapter dedicated to the micropolar theory.

Constitutive Equations

The deformation gradient is decomposed into elastic and plastic parts in the form,

$$\mathbf{F} = \mathbf{F}^e \ \mathbf{F}^p \tag{9}$$

The isoclinic intermediate configuration is defined in a unique way by keeping the crystal orientation unchanged from the initial to the intermediate configuration following Mandel (1973). The plastic distortion $\mathbf{F}^p$ is invariant with respect to rigid body motions that are carried by $\mathbf{F}^e$. The current mass density is ρ, whereas the mass density of the material element in the intermediate configuration is $\tilde{\rho}$, such that $\tilde{\rho}/\rho = J_e := \det(\mathbf{F}^e)$. The elastic strain is defined as:

$$\tilde{\mathbf{E}}^e := \frac{1}{2} \left(\mathbf{F}^{eT} \ \mathbf{F}^e - 1 \right) \tag{10}$$

The microdeformation is linked to the plastic deformation via the introduction of a relative deformation measure, defined as:

$$\mathbf{e}^p := \mathbf{F}^{p-1} \ \widehat{\boldsymbol{\chi}}^p - 1 \tag{11}$$

This tensor $\mathbf{e}^p$ measures the departure of the microdeformation from the plastic deformation. The state variables are assumed to be the elastic strain, the relative deformation, the curl of microdeformation, and some internal variables, α:

$$STATE := \left\{ \tilde{\mathbf{E}}^e, \mathbf{e}^p, \mathbf{K}, \alpha \right\} \tag{12}$$

The specific Helmholtz free energy density, ψ, is assumed to be a function of this set of state variables. In particular, in this simple version of the model, the curl of microdeformation is assumed to contribute entirely to the stored energy. In more sophisticated models, as proposed in Forest and Sievert (2003, 2006), Forest (2009), and Gurtin and Anand (2009), the relative deformation, the microdeformation, and its gradient can be split into elastic and plastic parts.

When the internal constraint $\mathbf{e}^p \equiv 0$ is enforced, the plastic microdeformation coincides with the plastic deformation so that the curl of the plastic microdeformation is directly related to the dislocation density tensor previously defined by:

$$\mathbf{K} := \mathrm{Curl} \; \widehat{\chi}^p \equiv \mathrm{Curl} \; \mathbf{F}^p = J\mathbf{A}\mathbf{F}^{-T} \tag{13}$$

where $\mathbf{A}$ is the dislocation density tensor defined as the curl of the inverse elastic deformation.

The micromorphic model then reduces to strain gradient plasticity according to Gurtin (2002).

The dissipation rate density is the difference:

$$\Delta^{intr} := p^{(i)} - \rho\dot{\psi} \geq 0 \tag{14}$$

which must be positive according to the second principle of thermodynamics. When the previous strain measures are introduced, the power density of internal forces takes the following form:

$$
\begin{aligned}
p^{(i)} &= \boldsymbol{\sigma} : \dot{\mathbf{F}}^e \mathbf{F}^{e-1} + \boldsymbol{\sigma} : \left(\mathbf{F}^e \; \dot{\mathbf{F}}^p \; \mathbf{F}^{p-1} \; \mathbf{F}^{e-1} \right) + \mathbf{s} : \left(\mathbf{F}^p \; \dot{\mathbf{e}}^p + \dot{\mathbf{F}}^p \; \mathbf{e}^p \right) + \mathbf{M} : \dot{\mathbf{K}} \; \mathbf{F}^{-1} \\
&= \frac{\rho}{\tilde{\rho}} \boldsymbol{\Pi}^e : \dot{\tilde{\mathbf{E}}}^e + \frac{\rho}{\tilde{\rho}} \boldsymbol{\Pi}^M : \dot{\mathbf{F}}^p \; \mathbf{F}^{p-1} + \mathbf{s} : \left(\mathbf{F}^p \; \dot{\mathbf{e}}^p + \dot{\mathbf{F}}^p \; \mathbf{e}^p \right) + \mathbf{M} : \dot{\mathbf{K}} \; \mathbf{F}^{-1}
\end{aligned}
\tag{15}
$$

where $\boldsymbol{\Pi}^e$ is the second Piola–Kirchhoff stress tensor with respect to the intermediate configuration and $\boldsymbol{\Pi}^M$ is the Mandel stress tensor:

$$\boldsymbol{\Pi}^e := J_e \; \mathbf{F}^{e-1} \; \boldsymbol{\sigma} \; \mathbf{F}^{e-T}, \; \boldsymbol{\Pi}^M := J_e \; \mathbf{F}^{eT} \; \boldsymbol{\sigma} \; \mathbf{F}^{e-T} = \mathbf{F}^{eT} \; \mathbf{F}^e \; \boldsymbol{\Pi}^e \tag{16}$$

On the other hand,

$$\rho\dot{\psi} = \rho \frac{\partial\psi}{\partial\tilde{\mathbf{E}}^e} : \dot{\tilde{\mathbf{E}}}^e + \rho \frac{\partial\psi}{\partial\mathbf{e}^p} : \dot{\mathbf{e}}^p + \rho \frac{\partial\psi}{\partial\mathbf{K}} : \dot{\mathbf{K}} + \rho \frac{\partial\psi}{\partial\alpha} \dot{\alpha} \tag{17}$$

We compute:

$$J_e D = \left(\mathbf{\Pi}^e - \tilde{\rho} \frac{\partial \psi}{\partial \tilde{\mathbf{E}}^e} \right) : \dot{\tilde{\mathbf{E}}}^e + \left(J_e \ \mathbf{F}^{pT} \mathbf{s} - \tilde{\rho} \frac{\partial \psi}{\partial \mathbf{e}^p} \right) : \dot{\mathbf{e}}^p$$

$$+ \left(J_e \mathbf{M} \ \mathbf{F}^{-T} - \tilde{\rho} \frac{\partial \psi}{\partial \mathbf{K}} \right) : \dot{\mathbf{K}} \tag{18}$$

$$+ \left(\mathbf{\Pi}^M + J_e \mathbf{s} \ \widehat{\boldsymbol{\chi}}^{pT} \right) : \dot{\mathbf{F}}^p \ \mathbf{F}^{p-1} - \tilde{\rho} \frac{\partial \psi}{\partial \alpha} \dot{\alpha} \geq 0$$

Assuming that the processes associated with $\dot{\tilde{\mathbf{E}}}^e$, $\dot{\mathbf{e}}^p$ and $\dot{\mathbf{K}}$ are nondissipative, the state laws are obtained:

$$\mathbf{\Pi}^e = \tilde{\rho} \frac{\partial \psi}{\partial \tilde{\mathbf{E}}^e}, \ \mathbf{s} = J_e^{-1} \ \mathbf{F}^{p-T} \ \tilde{\rho} \frac{\partial \psi}{\partial \mathbf{e}^p}, \ \mathbf{M} = J_e^{-1} \ \tilde{\rho} \frac{\partial \psi}{\partial \mathbf{K}} \ \mathbf{F}^T \tag{19}$$

The residual dissipation rate is:

$$J_e D = \left(\mathbf{\Pi}^M + J_e \mathbf{s} \ \widehat{\boldsymbol{\chi}}^{pT} \right) : \dot{\mathbf{F}}^p \ \mathbf{F}^{p-1} - R \dot{\alpha} \geq 0, \ \text{with } R := \tilde{\rho} \frac{\partial \psi}{\partial \alpha} \tag{20}$$

At this stage, a dissipation potential that depends on stress measures, $\Omega(S, R)$, is introduced in order to formulate the evolution equations for plastic flow and internal variables:

$$\dot{\mathbf{F}}^p \ \mathbf{F}^{p-1} = \frac{\partial \Omega}{\partial S}, \ \text{with } S := \mathbf{\Pi}^M + J_e \mathbf{s} \ \widehat{\boldsymbol{\chi}}^{pT} \tag{21}$$

$$\dot{\alpha} = -\frac{\partial \Omega}{\partial R} \tag{22}$$

where R is the thermodynamic force associated with the internal variable α and S is the effective stress conjugate to plastic strain rate, the driving force for plastic flow.

In the case of crystal plasticity, a generalized Schmid law is adopted for each slip system s in the form:

$$f^s \left(S, \tau_c^s \right) = |S : \mathbf{P}^s| - \tau_c^s \geq 0, \ \text{with } \mathbf{P}^s = \boldsymbol{l}^s \otimes \boldsymbol{n}^s \tag{23}$$

for activation of slip system s with slip direction, $\boldsymbol{l}^s$, and normal to the slip plane, $\boldsymbol{n}^s$. We call $\mathbf{P}^s$ the orientation tensor. The critical resolved shear stress is τ_c^s which may be a function of R in the presence of isotropic hardening. The kinematics of plastic slip follows from the choice of a dissipation potential, $\Omega(f^s)$, that depends on the stress variables through the yield function itself, f^s:

$$\dot{\mathbf{F}}^p \ \mathbf{F}^{p-1} = \sum_{s=1}^N \frac{\partial \Omega}{\partial f^s} \frac{\partial f^s}{\partial S} = \sum_{s=1}^N \dot{\gamma}^s \ \mathbf{P}^s, \ \text{with } \dot{\gamma}^s = \frac{\partial \Omega}{\partial f^s} \text{sign} \left(S : \mathbf{P}^s \right) \tag{24}$$

A possible viscoplastic potential is then:

$$\Omega\left(f^s\right) = \frac{K}{n+1} < \frac{f^s}{K} >^{n+1} \tag{25}$$

where K and n are viscosity parameters associated with viscoplastic slip, and the brackets stand for $< \cdot > = \mathrm{Max}(0, \cdot)$. The generalized resolved shear stress can be decomposed into two contributions:

$$\mathcal{S} : \mathbf{P}^s = \tau^s - x^s, \text{ with } \tau^s = \mathbf{\Pi}^M : \mathbf{P}^s \text{ and } x^s = -\mathbf{s}\,\widehat{\boldsymbol{\chi}}^{pT} : \mathbf{P}^s \tag{26}$$

The usual resolved shear stress is τ^s, whereas x^s can be interpreted as an internal stress or back stress leading to kinematic hardening. The fact that the introduction of the effect of the dislocation density tensor or, more generally, of gradient of plastic strain tensor leads to the existence of internal stresses induced by higher-order stresses has already been noticed by Steinmann (1996); see also Forest (2008). The back stress component is induced by the microstress $\mathbf{s}$ or, equivalently, by the curl of the generalized couple-stress tensor, $\mathbf{M}$, via the balance Eq. (7).

Geometrically Linearized Model

When deformations and rotations remain sufficiently small, the previous equations can be linearized as follows:

$$\mathbf{F} = 1 + \mathbf{H} \simeq 1 + \mathbf{H}^e + \mathbf{H}^p, \ \mathbf{H}^e = \boldsymbol{\varepsilon}^e + \boldsymbol{\omega}^e, \ \mathbf{H}^p = \boldsymbol{\varepsilon}^p + \boldsymbol{\omega}^p \tag{27}$$

where $\boldsymbol{\varepsilon}^e$ and $\boldsymbol{\omega}^e$ (resp. $\boldsymbol{\varepsilon}^p$, $\boldsymbol{\omega}^p$) are the symmetric and skew-symmetric parts of $\mathbf{F}^e - \mathbf{1}$ (resp. $\mathbf{F}^p - \mathbf{1}$). When microdeformation is small, the relative deformation is linearized as:

$$\mathbf{e}^p = \left(\mathbf{1} + \mathbf{H}^p\right)^{-1}\ \left(\mathbf{1} + \boldsymbol{\chi}^p\right) - \mathbf{1} \simeq \boldsymbol{\chi}^p - \mathbf{H}^p, \text{ with } \boldsymbol{\chi}^p = \widehat{\boldsymbol{\chi}}^p - \mathbf{1} \tag{28}$$

When linearized, the state laws (19) become:

$$\boldsymbol{\sigma} = \rho\frac{\partial\psi}{\partial\boldsymbol{\varepsilon}^e}, \ \mathbf{s} = \rho\frac{\partial\psi}{\partial\mathbf{e}^p}, \ \mathbf{M} = \rho\frac{\partial\psi}{\partial\mathbf{K}} \tag{29}$$

The evolution equations read then:

$$\dot{\boldsymbol{\varepsilon}}^p = \frac{\partial\Omega}{\partial\left(\boldsymbol{\sigma}+\mathbf{s}\right)}, \ \dot{\alpha} = -\frac{\partial\Omega}{\partial R} \tag{30}$$

The most simple case of a quadratic free energy potential is first considered:

$$\rho\psi\left(\boldsymbol{\varepsilon}^e, \mathbf{e}^p, \mathbf{K}\right) = \frac{1}{2}\boldsymbol{\varepsilon}^e : \mathbb{C} : \boldsymbol{\varepsilon}^e + \frac{1}{2}H_\chi\mathbf{e}^p : \mathbf{e}^p + \frac{1}{2}A\mathbf{K} : \mathbf{K} \tag{31}$$

The usual four-rank tensor of elastic moduli is denoted by $\mathbb{C}$. The higher-order moduli have been limited to only two additional parameters: H_χ (unit MPa) and A (unit MPa.mm^2). Their essential impact on the prediction of size effects will be analyzed in the next section. It follows that:

$$\boldsymbol{\sigma} = \boldsymbol{C} : \boldsymbol{\varepsilon}^e, \ \mathbf{s} = H_\chi \mathbf{e}^p, \ \mathbf{M} = A\boldsymbol{K} \tag{32}$$

Large values of H_χ ensure that $\mathbf{e}^p$ remains small so that $\widehat{\boldsymbol{\chi}}^p$ remains close to $\mathbf{H}^p$ and $\mathbf{K}$ is close to the dislocation density tensor. The yield condition for each slip system becomes:

$$f^s = |\tau^s - x^s| - \tau_c^s \tag{33}$$

with

$$x^s = -\mathbf{s} : \mathbf{P}^s = (\text{curl } \mathbf{M}) : \mathbf{P}^s = A\,(\text{curl } \text{curl } \boldsymbol{\chi}^p) : \mathbf{P}^s \tag{34}$$

Comparison Between Micropolar and Micromorphic Crystal Plasticity

Experimental techniques like Electron Back-Scatter Diffraction (EBSD) provide the field of lattice orientation and, consequently, of lattice rotation $\mathbf{R}^e$ during deformation. The rotation $\mathbf{R}^e$ appears in the polar decomposition of the elastic deformation $\mathbf{F}^e = \mathbf{R}^e \mathbf{U}^e$, where $\mathbf{U}^e$ is the lattice stretch tensor. Since

$$\boldsymbol{\alpha} = -\text{curl } \mathbf{F}^{e-1} = -\text{curl } \left(\mathbf{U}^{e-1} \cdot \mathbf{R}^{eT}\right) \tag{35}$$

the hypothesis of small elastic strain implies

$$\boldsymbol{\alpha} \simeq -\text{curl } \mathbf{R}^{eT} \tag{36}$$

This approximation also requires that the gradient of elastic strain is also small, which is not ensured even if the elastic strain is small. If, in addition, elastic rotations are small, we have:

$$\boldsymbol{\alpha} \simeq -\text{curl } (\mathbf{1} - \boldsymbol{\omega}^e) = \text{curl } \boldsymbol{\omega}^e \tag{37}$$

The small rotation axial vector is defined as:

$$\overset{\times_e}{\boldsymbol{\omega}} = -\frac{1}{2}\underline{\underline{\boldsymbol{\epsilon}}} : \boldsymbol{\omega}^e, \ \boldsymbol{\omega}^e = -\underline{\underline{\boldsymbol{\epsilon}}} \cdot \overset{\times_e}{\boldsymbol{\omega}} \tag{38}$$

or, in matrix notations:

$$[\omega^e] = \begin{bmatrix} 0 & \omega_{12}^e & -\omega_{31}^e \\ -\omega_{12}^e & 0 & \omega_{23}^e \\ \omega_{31}^e & -\omega_{23}^e & 0 \end{bmatrix} = \begin{bmatrix} 0 & -\overset{\times_e}{\omega}_3 & \overset{\times_e}{\omega}_2 \\ \overset{\times_e}{\omega}_3 & 0 & -\overset{\times_e}{\omega}_1 \\ -\overset{\times_e}{\omega}_2 & \overset{\times_e}{\omega}_1 & 0 \end{bmatrix} \tag{39}$$

The gradient of the lattice rotation field delivers the lattice curvature tensor. In the small deformation context, the gradient of the rotation tensor is represented by the gradient of the axial vector:

$$\boldsymbol{\kappa} := \overset{\times_e}{\boldsymbol{\omega}} \otimes \tag{40}$$

One can establish a direct link between curl $\boldsymbol{\omega}^e$ and the gradient of the axial vector associated with $\boldsymbol{\omega}$. For that purpose, the matrix form of curl $\boldsymbol{\omega}^e$ is derived according to:

$$[\text{curl } \boldsymbol{\omega}^e] = \begin{bmatrix} \omega_{12,3}^e + \omega_{31,2}^e & -\omega_{31,1}^e & -\omega_{12,1}^e \\ -\omega_{23,2}^e & \omega_{12,3}^e + \omega_{23,1}^e & -\omega_{12,2}^e \\ -\omega_{23,3}^e & -\omega_{31,3}^e & \omega_{23,1}^e + \omega_{31,2}^e \end{bmatrix} \tag{41}$$

or equivalently:

$$[\text{curl } \boldsymbol{\omega}^e] = \begin{bmatrix} -\overset{\times_e}{\omega}_{3,3} - \overset{\times_e}{\omega}_{2,2} & \overset{\times_e}{\omega}_{2,1} & \overset{\times}{\omega}_{3,1} \\ \overset{\times_e}{\omega}_{1,2} & -\overset{\times_e}{\omega}_{3,2} - \overset{\times_e}{\omega}_{1,1} & \overset{\times^e}{\omega}_{3,2} \\ \overset{\times_e}{\omega}_{1,3} & \overset{\times_e}{\omega}_{2,3} & -\overset{\times_e}{\omega}_{1,1} - \overset{\times_e}{\omega}_{2,2} \end{bmatrix} \tag{42}$$

from which it becomes apparent that:

$$\boldsymbol{\alpha} = \boldsymbol{\kappa}^T - (\text{trace } \boldsymbol{\kappa}) \, \mathbf{1}, \quad \boldsymbol{\kappa} = \boldsymbol{\alpha}^T - \frac{1}{2} (\text{trace } \boldsymbol{\alpha}) \, \mathbf{1} \tag{43}$$

This is a remarkable relation linking, with the context of small elastic strains (and in fact of small gradients of elastic strain) and rotations, the dislocation density tensor to lattice curvature. It is known as Nye's formula (Nye 1953).

As a conclusion, it appears that the Cosserat crystal plasticity model only considers the lattice curvature part contained in the full dislocation tensor. This seems to be a reasonable assumption. However, some significant differences can be found in the predictions of Cosserat vs. full micromorphic theory, as discussed in the reference Cordero et al. (2010a).
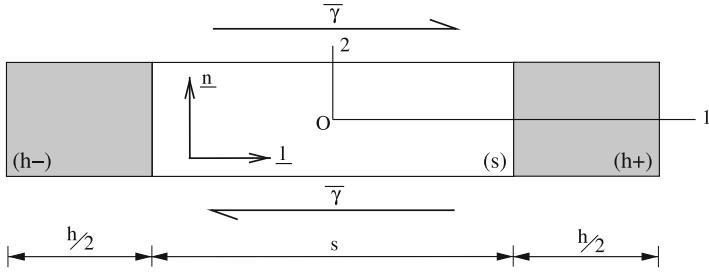
Fig. 1 Single slip in a periodic two-phase single-crystal laminate under simple shear: the gray phase (h) displays a purely linear elastic behavior, whereas the inelastic deformation of the white elasto-plastic phase (s) is controlled by a single-slip system (n, l)

Size Effects in a Two-Phase Single-Crystal Laminate

A periodic two-phase single-crystal laminate under simple shear, whose unit cell is shown in Fig. 1, is considered, following Forest and Sedláček (2003a), Forest (2008), and Cordero et al. (2010a). This microstructure is composed of a hard elastic phase (h) and a soft elasto-plastic phase (s) where one slip system with slip direction normal to the interface between (h) and (s) is chosen. A mean simple glide $\overline{\gamma}$ is applied in the crystal slip direction l of the phase (s). The displacement and microdeformation fields take the form:

$$u_1 = \overline{\gamma} x_2, \; u_2\left(x_1\right), \; u_3 = 0, \; \chi^p_{12}\left(x_1\right), \; \chi^p_{21}\left(x_1\right) \tag{44}$$

within the context of small deformation theory. It follows that:

$$[\mathbf{H}] = \begin{bmatrix} 0 & \overline{\gamma} & 0 \\ u_{2,1} & 0 & 0 \\ 0 & 0 & 0 \end{bmatrix}$$

$$[\mathbf{H}^p] = \begin{bmatrix} 0 & \gamma & 0 \\ 0 & 0 & 0 \\ 0 & 0 & 0 \end{bmatrix} \; [\mathbf{H}^e] = \begin{bmatrix} 0 & \overline{\gamma} - \gamma & 0 \\ u_{2,1} & 0 & 0 \\ 0 & 0 & 0 \end{bmatrix}$$

$$[\chi^p] = \begin{bmatrix} 0 & \chi^p_{12}\left(x_1\right) & 0 \\ \chi^p_{21}\left(x_1\right) & 0 & 0 \\ 0 & 0 & 0 \end{bmatrix} \; [\text{curl } \chi^p] = \begin{bmatrix} 0 & 0 & -\chi^p_{12,1} \\ 0 & 0 & 0 \\ 0 & 0 & 0 \end{bmatrix}$$

The resulting stress tensors are:

$$[\sigma] = \mu \begin{bmatrix} 0 & \overline{\gamma} - \gamma + u_{2,1} & 0 \\ \overline{\gamma} - \gamma + u_{2,1} & 0 & 0 \\ 0 & 0 & 0 \end{bmatrix}$$

$$[s] = -H_\chi \begin{bmatrix} 0 & \gamma - \chi_{12}^p & 0 \\ -\chi_{21}^p & 0 & 0 \\ 0 & 0 & 0 \end{bmatrix}$$

$$[M] = \begin{bmatrix} 0 & 0 & -A\chi_{12,1}^p \\ 0 & 0 & 0 \\ 0 & 0 & 0 \end{bmatrix} \quad [\text{curl } M] = \begin{bmatrix} 0 & -A\chi_{12,11}^p & 0 \\ 0 & 0 & 0 \\ 0 & 0 & 0 \end{bmatrix}$$

These forms of matrices are valid for both phases, except that $\gamma \equiv 0$ in the hard elastic phase. Each phase possesses its own material parameters, H_χ and A, the shear modulus, μ, being assumed for simplicity to be identical in both phases. The balance equation, $s = -\text{curl } M$, gives $\chi_{21}^p = 0$ and the plastic slip:

$$\gamma = \chi_{12}^p - \frac{A}{H_\chi} \chi_{12,11}^p. \tag{45}$$

In the soft phase, the plasticity criterion stipulates that:

$$\sigma_{12} + s_{12} = \tau_c + H\gamma_{\text{cum}}, \tag{46}$$

where H is a linear hardening modulus considered in this phase and γ_{cum} is the accumulated plastic slip as $\dot{\gamma}_{\text{cum}} = |\dot{\gamma}|$. The following analytical resolution is done for the first loading branch, under monotonic loading. The slip direction, l, has been chosen such that $\gamma > 0$ for this first loading branch so that we have: $\gamma_{\text{cum}} = \gamma$. Considering Eqs. (45) and (46), we obtain the second-order differential equation for the microdeformation variable in the soft phase, χ_{12}^{ps},

$$\frac{1}{\omega^{s2}} \chi_{12,11}^{ps} - \chi_{12}^{ps} = \frac{\tau_c - \sigma_{12}}{H}, \text{ with } \omega^s = \sqrt{\frac{H_\chi^s H}{A^s \left(H_\chi^s + H \right)}}. \tag{47}$$

where $1/\omega^s$ is the characteristic length of the soft phase for this boundary value problem. The force stress balance equation requires σ_{12} to be uniform. It follows that the nonhomogeneous part of the differential equation is constant and then the hyperbolic profile of χ_{12}^{ps} takes the form:

$$\chi_{12}^{ps} = C^s \cosh (\omega^s x) + D, \tag{48}$$

where C^s and D are constants to be determined. Symmetry conditions $\left(\chi_{12}^{ps} (-s/2) = \chi_{12}^{ps} (s/2) \right)$ have been taken into account.

In the elastic phase, where the plastic slip vanishes, a hyperbolic profile of the microdeformation variable, χ_{12}^{ph}, is also obtained:

$$\chi_{12}^{ph} = C^h \cosh\left(\omega^h \left(x \pm \frac{s+h}{2}\right)\right), \text{ with } \omega^h = \sqrt{\frac{H_\chi^h}{A^h}}, \qquad (49)$$

where, again, C^h is a constant to be determined, and symmetry conditions have been taken into account. It is remarkable that the plastic microvariable, χ_{12}^{ph}, does not vanish in the elastic phase, close to the interfaces, although no plastic deformation takes place. This is due to the transmission of double traction. Such a transmission has been shown in Cordero et al. (2010a) to be essential for size effects to occur. This point will be discussed in section "Size Effects in a Two-Phase Single-Crystal Laminate." The linear constitutive equation for the double-stress tensor in (32) can be interpreted, for the elastic phase, as nonlocal elasticity. That is why the corresponding characteristic length, $1/\omega^h$, will be kept of the order of nanometers in the presented simulation.

The coefficients C^s, D, and C^h can be identified using the interface and periodicity conditions:

- Continuity of χ_{12}^p at $x = \pm s/2$:

$$C^s \cosh\left(\omega^s \frac{s}{2}\right) + D = C^h \cosh\left(\omega^h \frac{h}{2}\right). \qquad (50)$$

- Continuity of the double traction, as given in Eq. (8), $m_{12} = -M_{13}$ at $x = \pm s/2$:

$$A^s \omega^s C^s \sinh\left(\omega^s \frac{s}{2}\right) = -A^h \omega^h C^h \sinh\left(\omega^h \frac{h}{2}\right). \qquad (51)$$

- Periodicity of displacement component u_2. We have the constant stress component:

$$\sigma_{12} = \mu \left(\overline{\gamma} - \gamma + u_{2,1}\right) \qquad (52)$$

whose value is obtained from the plasticity criterion in the soft phase (Eq. 46):

$$\sigma_{12} = \tau_c + H\gamma_{cum} - A^s \chi_{12,11}^{ps}. \qquad (53)$$

Still considering the first loading branch for which $\gamma_{cum} = \gamma$, it follows that:

$$u_{2,1}^s = \frac{\sigma_{12}}{\mu} - \overline{\gamma} + \gamma = \frac{\tau_c}{\mu} - \overline{\gamma} + \frac{A^s \omega^{s2} C^s}{H} \cosh\left(\omega^s x\right) + \frac{H+\mu}{\mu} D \qquad (54)$$

in the soft phase and:
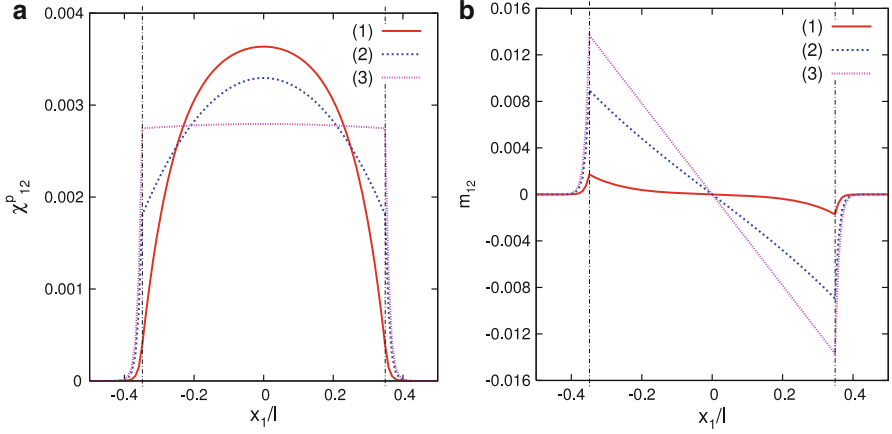
Fig. 2 Profiles of (**a**) plastic microdeformation χ^p_{12} and (**b**) double traction m_{12} in the two-phase microstructure with the *microcurl* model at 0.2% overall plastic strain obtained with the set of material parameters given in Table 1 and (1) with no mismatch between the moduli of the two phases, $A^h = A^s = 5.10^{-5}$ MPa.mm^2; (2) with a stronger mismatch, $A^h = 5.10^{-5}$ MPa.mm^2 and $A^s = 1.10^{-3}$ MPa.mm^2; and (3) $A^h = 5.10^{-5}$ MPa.mm^2 and $A^s = 5.10^{-2}$ MPa.mm^2. The associated intrinsic length scales, $1/\omega^s$, are, respectively, 100 nm, 449 nm, and 3.2 μm. In all three cases, the fraction of soft phase $f_s = 0.7$ and the microstructure size is fixed, $l = 1$ μm. The *vertical lines* indicate the position of interfaces

$$u^h_{2,1} = \frac{\sigma_{12}}{\mu} - \overline{\gamma} = \frac{\tau_c}{\mu} - \overline{\gamma} + \frac{H}{\mu} D \tag{55}$$

in the hard phase. The average on the whole structure,

$$\int_{-(s+h)/2}^{(s+h)/2} u_{2,1} dx = 0, \tag{56}$$

must vanish for periodicity reasons and gives

$$\left(\frac{\tau_c}{\mu} - \overline{\gamma} \right)(s + h) + \frac{2A^s \omega^s C^s}{H} \sinh \left(\omega^s \frac{s}{2} \right) + \frac{H(s+h) + \mu s}{\mu} D = 0 \tag{57}$$

The resolution of Eqs. (50), (51), and (57) gives:

$$C^s = \left(\frac{\tau_c}{\mu} - \overline{\gamma} \right)$$

$$\left[\frac{A^s \omega^s \sinh \left(\omega^s \frac{s}{2} \right)}{s + h} \left(\frac{H(s+h) + \mu s}{\mu} \left(\frac{\coth \left(\omega^s \frac{s}{2} \right)}{A^s \omega^s} + \frac{\coth \left(\omega^h \frac{h}{2} \right)}{A^h \omega^h} \right) - \frac{2}{H} \right) \right]^{-1} \tag{58}$$

Table 1 Set of material parameters used in the simulations. The intrinsic length scales, defined as $1/\omega^{h,s}$, induced by these parameters is of the order of 10 nm for the elastic phase (h) and 500 nm for the plastic phase (s)

	μ[MPa]	τ_c[MPa]	H[MPa]	H_χ[MPa]	A[MPa.mm^2]
Phase (s)	35,000	40	5000	500,000	1.10^{-3}
Phase (h)	35,000	–	–	500,000	5.10^{-5}

$$D = -A^s \omega^s C^s \sinh\left(\omega^s \frac{s}{2}\right) \left(\frac{\coth\left(\omega^s \frac{s}{2}\right)}{A^s \omega^s} + \frac{\coth\left(\omega^h \frac{h}{2}\right)}{A^h \omega^h} \right) \tag{59}$$

$$C^h = -C^s \frac{A^s \omega^s \sinh\left(\omega^s \frac{s}{2}\right)}{A^h \omega^h \sinh\left(\omega^h \frac{h}{2}\right)}. \tag{60}$$

Figure 2 shows the profiles of plastic microdeformation and double traction in the two-phase laminate for different sets of material parameters and for a fraction of soft phase (s), $f_s = 0.7$. These profiles clearly show the continuity of χ_{12}^p and m_{12} at the interfaces. The different shapes presented are obtained for various values of the modulus A^s, the other material parameters being fixed and given in Table 1. Varying A^s modifies the mismatch with respect to the modulus A^h of the phase (h). Without mismatch the profile of χ_{12}^p is smooth at interfaces, while stronger mismatches lead to sharper transitions between the phases. Varying A^s also changes the intrinsic length scale $1/\omega^s$ of the phase (s). When the intrinsic length scale is small compared to the size of the microstructure, the microdeformation gradient can develop inside the phase (s) which leads to a rounded profile of the plastic microdeformation χ_{12}^p and to a double traction m_{12} localized at the interfaces. When the intrinsic length scale increases, the value of the double traction also increases at the interfaces (or equivalently, when decreasing the microstructure length scale, $l = s + h$, for a fixed intrinsic length scale). When the intrinsic length scale becomes of the order of the size of the microstructure or even larger, the model starts to saturate so that χ_{12}^p becomes quasihomogeneous (flat profile) and the double traction is not localized anymore (linear profile). From Eq. (53) we derive the expression of the macroscopic stress tensor component, Σ_{12}, defined as the mean value of the stress component σ_{12} over the microstructure size, $l = (s + h)$:

$$\Sigma_{12} = \langle\sigma_{12}\rangle = \frac{1}{l} \int_{-\frac{1}{2}}^{\frac{1}{2}} \sigma_{12} dx = \tau_c + \frac{H}{f_s}\langle\gamma^{cum}\rangle - \frac{A^s}{f_s}\langle\chi_{12,11}^{ps}\rangle, \tag{61}$$

where brackets $<>$ denote the average values over the microstructure unit cell. We obtain the mean plastic slip for the first loading branch from Eq. (45):

$$\langle \gamma \rangle = \left\langle \chi_{12}^{ps} - \frac{A^s}{H_\chi^s} \chi_{12,11}^{ps} \right\rangle = \frac{2 A^s \omega^s C^s \sinh\left(\omega^s \frac{f_s l}{2}\right)}{H l} + f_s D \tag{62}$$

where f_s is the fraction of soft phase. From this we obtain alternative expressions of C^s and D as functions of $\langle \gamma \rangle$,

$$C^s = -\langle \gamma \rangle$$

$$\left[A^s \omega^s \sinh\left(\omega^s \frac{f_s l}{2}\right) \left(f_s \left(\frac{\coth\left(\omega^s \frac{f_s l}{2}\right)}{A^s \omega^s} + \frac{\coth\left(\omega^h \frac{(1-f_s)l}{2}\right)}{A^h \omega^h} \right) - \frac{2}{H l} \right) \right]^{-1} \tag{63}$$

$$D = \langle \gamma \rangle \left[f_s - \frac{2}{H l} \left(\frac{\coth\left(\omega^s \frac{f_s l}{2}\right)}{A^s \omega^s} + \frac{\coth\left(\omega^h \frac{(1-f_s)l}{2}\right)}{A^h \omega^h} \right)^{-1} \right]^{-1} \tag{64}$$

which contain contributions from both the back stress and the isotropic hardening. The macroscopic stress takes the form:

$$\sum_{12} = \tau_c + H D. \tag{65}$$

The hardening produced by the model is a combination of the kinematic hardening arising from the higher-order back stress component and the linear isotropic hardening introduced in (46). Its modulus, H^{tot}, is size-dependent and is obtained using Eqs. (64) and (65):

$$H^{tot} = H \left[f_s - \frac{2}{H l} \left(\frac{\coth\left(\omega^s \frac{f_s l}{2}\right)}{A^s \omega^s} + \frac{\coth\left(\omega^h \frac{(1-f_s)l}{2}\right)}{A^h \omega^h} \right)^{-1} \right]^{-1} \tag{66}$$

One cycle of deformation $\bar{\gamma}$ has been considered to illustrate the kinematic hardening effects. In the absence of gradient effects, only isotropic hardening is visible. The *microcurl* model leads to an additional kinematic hardening component. When the size of the elasto-plastic phase (s) becomes large compared to the intrinsic length scale $1/\omega_s$, strain gradient effect is small, and the kinematic hardening arising from the *microcurl* model tends to vanish. Then the model reduces to conventional crystal plasticity theory, and the limit of the 0.2% macroscopic flow stress is:

$$\lim_{l \to \infty} \sum_{12|0.2} = \tau_c + \frac{H}{f_s} \langle \gamma^{cum} \rangle. \tag{67}$$

In contrast, the maximum extra stress, $\Delta\Sigma$, predicted by the model at small microstructure sizes can be computed as:

$$\Delta\Sigma = \lim_{l\to 0}\sum_{12}\left(\langle\gamma\rangle\right) - \lim_{l\to\infty}\sum_{12|0.2} = \frac{1-f_s}{f_s}H_\chi\langle\gamma\rangle. \tag{68}$$

Figure 3 presents the predicted evolution of the macroscopic flow stress $\Sigma_{12|0.2}$ at 0.2% plastic strain (obtained by setting $\langle\gamma\rangle = 0.002$) as a function of the microstructure length scale l in a log–log diagram. This evolution is plotted using the material parameters given in Table 1 and for various values of the coupling modulus, $H_\chi^s = H_\chi^h = H_\chi$. The four lower curves are obtained for finite values of the modulus H_χ; they exhibit a tanh shape with saturation for large ($l > 10^{-2}$ mm) and small ($l < 10^{-5}$ mm) values of l. These saturations can be characterized by the limit given in Eq. (67) and the maximum extra stress, $\Delta\Sigma$, given in Eq. (68), respectively. A transition domain with strong size dependence is observed between these two plateaus. The limits and the maximum extra stress, the position of the transition zone, and the scaling law exponent in the size-dependent domain (slope in the log–log diagram) are directly related to the material parameters used in the model. In fact, the position of the size-dependent domain is controlled by the moduli $A^{h,s}$ (not illustrated here), while the maximum extra stress and the scaling law exponent are both controlled by the modulus H_χ, both increasing for higher values of H_χ as suggested by Fig. 3.

When H_χ is very small, we can deduce from Eq. (68) that $\Delta\Sigma$ vanishes, and consequently the scaling law exponent will tend to 0. The upper curve is obtained for $H_\chi \to \infty$; it no longer exhibits a tanh shape as no saturation occurs for small values of l, the limit $\Delta\Sigma \to\infty$ follows. This limit case will be described in the next subsection; it will be shown that in that case, a scaling law exponent of -2 is reached. Finally, the *microcurl* model can produce scaling law exponents ranging from 0 to -2.

Strain Gradient Plasticity as a Limit Case

In the proposed *microcurl* model, the modulus H_χ introduces a coupling between micro and macro variables. A high value of H_χ forces the plastic microdeformation χ^p to remain as close as possible to the macroplastic deformation $\mathbf{H}^p$. Consequently, it enforces the condition that $\mathbf{K}$ coincides with the dislocation density tensor. In this case, the *microcurl* model degenerates into the strain gradient plasticity model by Gurtin (2002). When applied to the laminate microstructure, the strain gradient plasticity model leads to the indeterminacy of the double-traction vector at the interfaces, due to the fact that no strain gradient effect occurs in the elastic phase; see Cordero et al. (2010a). The *microcurl* model can then be used to derive the missing interface condition to be applied at the interface, by means of a limit process in the previous solution of the boundary value problem.
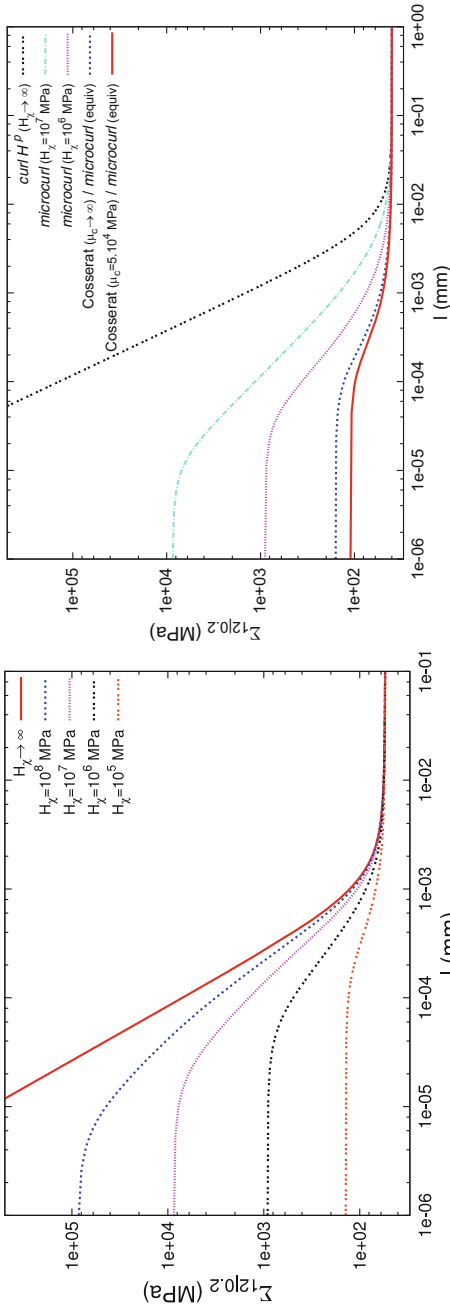
Fig. 3 Evolution of the macroscopic flow stress $\Sigma_{12|0.2}$ at 0.2% plastic strain as a function of the microstructure length scale l, plotted for different coupling moduli, $H_\chi \left(= H_\chi^s = H_\chi^h \right)$, on the left. The other material parameters are given in Table 1 and $f_s = 0.7$. On the right, comparison between the micropolar and micromorphic models

The limit $H_\chi \to \infty$ of the *microcurl* model can be used to determine the value of the double traction to be imposed at the interface, as follows:

$$\lim_{H_\chi \to \infty} m_{12}\,(s/2) = \lim_{H_\chi \to \infty} A^s \chi_{12,1}^{ps}\,(s/2)$$

$$= \lim_{H_\chi \to \infty} A^s \omega^s \sinh\left(\omega^s \frac{f_s l}{2}\right) C^s$$

$$= \lim_{H_\chi \to \infty} \langle \gamma \rangle \left[\frac{2}{Hl} - f_s \left(\frac{\coth\left(\omega^s \frac{f_s l}{2}\right)}{A^s \omega^s} + \frac{\coth\left(\omega^h \frac{(1-f_s)l}{2}\right)}{A^h \omega^h} \right) \right]^{-1}$$

Since $H_\chi \to \infty$, $1/\omega^h \to 0$ and $\coth(\omega^h h/2) \to 1$. Moreover, $\omega_\infty^s := \omega^s \to \sqrt{H/A^s}$.

Consequently,

$$\lim_{H_\chi \to \infty} m_{12}\,(s/2) = \langle \gamma \rangle \left[\frac{2}{Hl} - f_s \frac{\coth\left(\omega_\infty^s \frac{f_s l}{2}\right)}{A^s \omega_\infty^s} \right]^{-1} \tag{69}$$

Accordingly, the double traction is found to depend on the mean plastic slip. The characteristic length in the soft phase for the strain gradient plasticity model is found to be related to the ratio between the hardening modulus and the higher-order modulus, A^s. The limiting process can also be used to predict the response of the strain gradient plasticity model in the size effect zone. For that purpose, let us consider the limit of $\Sigma_{12|0\cdot 2}$, when H_χ goes to infinity. Indeed, when H_χ tends to infinity, the expression of D in Eq. (64) can be simplified. We consider sizes of the microstructures in the size effect zone, i.e., intermediate values of l. Since H_χ is very high, the term $\tanh(\omega^h(1-f_s)l/2)$ tends to 1. Considering that l is small enough, the term $l\,(\tanh(\omega_s f_s l/2))$ can be approximated by its Taylor expansion at the order 2, which leads to D of the form:

$$D \approx \frac{al + b}{cl^2 + dl + e} \tag{70}$$

where

$$a = \frac{\langle \gamma \rangle\, f_s}{2\sqrt{H_\chi}}, \quad b = \langle \gamma \rangle\, f_s A^h \left(1 + \frac{H}{H_\chi}\right) \tag{71}$$

$$c = -\frac{f_s^3 H \sqrt{A^h}}{12}, \quad d = \frac{f_s^2 H}{2\sqrt{H_\chi}}, \quad e = -\frac{f_s \sqrt{A^h}\, H}{H_\chi} \tag{72}$$

The terms a, d, and e tend to 0 when $H_\chi \to \infty$, so that:

$$D \approx \frac{12 A_s \langle \gamma \rangle}{f_s^3 H l^2} \tag{73}$$

and for the macroscopic stress:

$$\Sigma_{12} \approx \tau_c + \frac{12 A_s \langle \gamma \rangle}{f_s^3 l^2} \tag{74}$$

This expression indicates a l^{-2} scaling law for the strain gradient plasticity model. This scaling law differs from the Hall–Petch relation, $l^{-1/2}$, typical for grain size effects, and from the Orowan relation, l^{-1}, valid for precipitate size effects.

On the right Fig. 3 shows a comparison between the micropolar and micromorphic responses in the case of the two-phase laminate under shear. A saturation of the stress level is found for increasing values of the penalty modulus H_χ in the micropolar model at small scales. In contrast, the micromorphic response converges toward that of the strain gradient plasticity model and displays no limit at small scales. This is a fundamental difference between the lattice curvature-based and the dislocation density tensor-based models; see Cordero et al. (2010a).

Free Energy Potentials for Micromorphic Crystal Plasticity

The previous example showing that a simple quadratic potential with respect to the dislocation density tensor does not provide the satisfactory scaling law for the plastic behavior of the channel is an incentive for developing more physical constitutive laws for strain gradient plasticity. Such an attempt is presented in this section along the lines of Wulfinghoff et al. (2015).

Physically, the introduction of additional energy density terms may be motivated by the incomplete nature of the continuum theory. Clearly, the continuum description does not contain the full information on the discrete dislocation microstructure. In particular, single dislocations are not resolved. Instead, the continuum representation may be interpreted as a smoothed version of the real system, where information is lost deliberately. There is no reason to assume that the total elastic energy of the continuum representation coincides with the elastic energy of the real system including discrete dislocations. This is due to the loss of information as a result of the smoothing procedure (Mesarovic et al. 2010). Additional energy terms in gradient plasticity may therefore be interpreted as an attempt to partially compensate the error in the continuum elastic energy. This is done by taking into account available kinematical information on the dislocation microstructure as additional argument of the energy.

The optimal form of the energy is subject of current research. Most applications are based on a pragmatic quadratic approach (e.g., Cordero et al. 2012; Reddy et al. 2012; Wulfinghoff and Böhlke 2012; Miehe et al. 2014; Wulfinghoff et al. 2013a, b; Mesarovic et al. 2015).

Instead, a more reasonable approach seems to be based on a variable internal length scale as a function of the dislocation state (Groma et al. 2003; Mesarovic et al. 2010). The quadratic form was recently shown to provide physically unrealistic scaling in the size-dependent response of laminate microstructures under shear (Cordero et al. 2010b; Forest and Guéninchault 2013). Since quadratic forms are unusual in the classical dislocation theory, alternative free energy potentials were proposed in the past 10 years. Rank-one energies that are linear with respect to the GND densities have been shown to lead to a size-dependent yield stress in certain situations. Additionally motivated by line tension (and more elaborate) arguments, they are used by several authors (Ortiz and Repetto 1999; Conti and Ortiz 2005; Ohno and Okumura 2007; Kametani et al. 2012; Hurtado and Ortiz 2013).

Asymptotic methods can be used to derive alternative effective potential for distributions of edge dislocations. The asymptotic derivation of a logarithmic potential by De Luca et al. (2012) accounts for line tension effects at the macroscopic scale. Systematic derivations of back stress distributions were derived in Geers et al. (2013) by means of asymptotic methods.

The choice of a logarithmic energy is inspired by the statistical theory of dislocations of Groma et al. (2003, 2007) and Berdichevsky (2006a,b). Here, the internal length scale of the back stress is determined by the dislocation microstructure (see also Svendsen and Bargmann 2010; Forest and Guéninchault 2013). In the latter reference, the rank-one and logarithmic formulations were applied to strain gradient plasticity theories involving the full dislocation density tensor instead of the individual GND densities.

Formulation of Two Free Energy Potentials

It is assumed that the volumetric stored energy density has the form:

$$\rho \psi = W = W_e + W_g + W_h, \tag{75}$$

with $W_e = (\varepsilon - \varepsilon^p) : \mathbb{C} : (\varepsilon - \varepsilon^p)/2$. The expressions W_h and W_g are assumed to be functions of internal (hardening) variables α and the dislocation density tensor $\mathbf{A}$, respectively.

Size-independent isotropic hardening is accounted for by W_h, while W_g models size effects.

The following defect energies are investigated:

$$W_g^1 = c\,Gb\,\|\mathbf{A}\|, \quad W_g^{\ln} = c_0\,\|\mathbf{A}\|\,\ln\frac{\|\mathbf{A}\|}{A_0}, \tag{76}$$

where c is a constant of order unity, G is the macroscopic shear modulus, b is the Burgers vector, A_0 is a constant, and c_0 is given by:

$$c_0 = \frac{Gb\beta}{2\pi(1-\nu)}, \tag{77}$$

where ν is Poisson's ratio and β is of order unity. The Euclidean norm of the dislocation density tensor is defined as: $\|\mathbf{A}\| = \sqrt{\mathbf{A} \cdot \mathbf{A}}$.

The rank-one energy W_g^1 can be motivated by simple line tension arguments; see Ortiz and Repetto (1999) and Hurtado and Ortiz (2012, 2013).

The logarithmic energy $W_g^{\ln}$ (Eq. (76)) is motivated by the form of the associated back stress (Forest and Guéninchault 2013). It turns out that the approach $W_g^{\ln}$ leads to a back stress which is formally close to the one derived in the statistical theory of Groma et al. (2003), given in 1D by

$$\frac{Gc_1}{2\pi(1-\nu)\rho}\partial_{x_1}^2\gamma \tag{78}$$

for a single-slip situation with slip direction e_1. Here, ρ denotes the total dislocation density. In the two-dimensional single-slip regime, the back stress involves the Laplacian of the plastic slip, as postulated by Aifantis (1987). However, the internal length scale is not interpreted as a material constant but determined by the dislocation microstructure, if $W_g^{\ln}$ is applied.

The stresses σ and $\mathbf{M}$ are assumed to be energetic, i.e.,

$$\boldsymbol{\sigma} = \frac{\partial W}{\partial \boldsymbol{\varepsilon}^e}, \ \boldsymbol{M} = \frac{\partial W}{\partial \mathbf{A}} \tag{79}$$

If the stored energy is not differentiable at $\mathbf{A} = \mathbf{0}$, the symbol ∂ in Eq. (79)$_2$ is interpreted as a subdifferential operator (see, e.g., Han and Reddy 2013), i.e.,

$$\boldsymbol{M}|_{\alpha=0} \in \left\{ \boldsymbol{M} : W_g(\mathbf{A}) - \boldsymbol{M} \cdot \mathbf{A} \geq 0 \ \forall \mathbf{A} \right\}. \tag{80}$$

This can be interpreted as follows. If the stress $\boldsymbol{M}$ is applied at a material point, $\mathbf{A}$ will take a value which minimizes the expression $W_g(\mathbf{A}) - \mathbf{M} \cdot \mathbf{A}$. For small values of $\boldsymbol{M}$, the minimum is given by $\mathbf{A} = 0$. However, for sufficiently large values of $\boldsymbol{M}$, the value of $\mathbf{A}$ can be determined from the stationarity condition $\boldsymbol{M} = \partial_\alpha W_g$.

For example, if W_g is given by $W_g^1 = cGb\|\mathbf{A}\|$, it follows that $\mathbf{A} = 0$ if

$$\boldsymbol{M} : \mathbf{A} \leq W_g^1(\mathbf{A}) = cGb\|\mathbf{A}\| \ \forall \mathbf{A} \iff \boldsymbol{M} : \mathbf{A} \leq \|\boldsymbol{M}\|\|\mathbf{A}\| \leq cGb\|\mathbf{A}\| \ \forall \mathbf{A}. \tag{81}$$

Hence, it is found that:

$$\begin{cases} \boldsymbol{M} \in \{\boldsymbol{M} : \varphi(\boldsymbol{M}) \leq 0\}, \text{if } \mathbf{A} = 0 \\ \quad \boldsymbol{M} = cGb\frac{\mathbf{A}}{\|\mathbf{A}\|}, \text{else.} \end{cases} \tag{82}$$

with $\varphi(\boldsymbol{M}) = \|\boldsymbol{M}\| - cGb$.

Note that the generalized stress M can be computed uniquely from $\mathbf{A}$ only if $\mathbf{A} \neq 0$. This makes analytical solutions as well as the numerical implementation difficult. Possible numerical strategies concerning this problem are discussed in Kametani et al. (2012) as well as Hurtado and Ortiz (2013).

Application to the Shearing of the Periodic Laminate

In this section, the two new potentials are applied to the elasto-plastic laminate microstructure already considered in section "Size Effects in a Two-Phase Single-Crystal Laminate"; see Fig. 1. The two promising candidates of the defect energy function W_g are investigated concerning their effect on the overall size effects as well as the dislocation pileup structures building up at impenetrable boundaries. The dislocation density tensor can be expressed in terms of the edge density $\rho_\perp = -\partial_{x1}\gamma$

$$\mathbf{A} = -\rho_\perp \boldsymbol{e}_1 \otimes \boldsymbol{e}_3. \tag{83}$$

The quantity $\rho_\perp$ represents the total Burgers vector amount per unit area of edge dislocations. Note that its unit (μm^{-1}) differs from the unit of the total line length per unit volume ρ, given by μm^{-2}.

Assuming the defect energy W_g to be a function of $||\mathbf{A}||$, the generalized stress M reads

$$\boldsymbol{M} = \partial_A W_g = \partial_{\|A\|} W_g \frac{\mathbf{A}}{\|\mathbf{A}\|} = M(x_1)\,\boldsymbol{e}_1 \otimes \boldsymbol{e}_3. \tag{84}$$

From the balance Eq. $(7)_2$, it follows that

$$s_{12} - M' = 0. \tag{85}$$

Throughout this section, the isotropic hardening contribution will be neglected, i.e., $W_h = 0$.

Rank-One Defect Energy
For the laminate, the following energy is adopted:

$$W_g^1 = cGb\,\|\mathbf{A}\| = cGb\,|\rho_\perp|, \tag{86}$$

where c is of order unity (Ortiz and Repetto 1999). According to Eq. (84), the generalized stress M reads:

$$M = -\frac{\rho_\perp}{|\rho_\perp|}cGb = -\text{sign}\ \rho_\perp cGb, \text{ if } |\rho_\perp| > 0$$
$$|M| \leq cGb, \text{ if } |\rho_\perp| = 0 \tag{87}$$

where the second line follows from Eq. (82).

Subsequently, a monotonic shear deformation in the positive direction is prescribed such that the following relations hold in the soft phase: $\tau^{\text{eff}} \geq \tau^C, \quad \dot{\gamma} \geq 0$.

The principle of virtual power is written for the real field on the laminate unit cell V:

$$\int_V \boldsymbol{\sigma} : \dot{\boldsymbol{\varepsilon}} + \mathrm{s} : \dot{\mathbf{H}}^p + \mathbf{M} : \operatorname{curl} \dot{\mathbf{H}}^p dV = \int_{\partial V} \boldsymbol{t} \cdot \dot{\boldsymbol{u}} \, dS + \mathbf{m} : \dot{\mathbf{H}}^p dS \qquad (88)$$

The last term of the right-hand side vanishes due to the fact that $\mathbf{H}^p$ is periodic, whereas $\mathbf{m}$ is antiperiodic. The first term of the right-hand side coincides with the first term in the left-hand side, as can be shown by means of the Gauss theorem. As a result we obtain,

$$\int_{\partial V} \mathrm{s} : \dot{\mathbf{H}}^p + \mathbf{M} : \operatorname{curl} \dot{\mathbf{H}}^p \, dV = 0 \qquad (89)$$

For the laminate under single slip, this gives:

$$\int_{-s/2}^{s/2+h} s_{12} \, \dot{\gamma} + (-c \, Gb \operatorname{sign} \gamma_{,1}) \, (-\dot{\gamma}_{,1}) \, dx_1 = 0 \qquad (90)$$

Under monotonic loading, sign $\gamma_{,1}$ = sign $\dot{\gamma}_{,1}$, so that

$$\int_{-s/2}^{s/2+h} s_{12} \, \dot{\gamma} + c \, Gb \, |\dot{\gamma}_{,1}| \, dx_1 = 0 \qquad (91)$$

According to the Schmid law, $\sigma_{12} + s_{12} = \tau^{rmC}$ where the fields σ_{12}, s_{12} are uniform. The solution is such that the plastic slip field $\gamma(x_1)$ is uniform in $]-s/2, s/2[$ at each instant. So does $\dot{\gamma}(x_1) = \dot{\gamma}(0)$ in $]-s/2, s/2[$. It vanishes in $]s/2, s/2 + h[$. It is therefore discontinuous at $\pm s/2$. As a result, the derivative of the plastic slip rate is the sum of two Dirac functions:

$$\dot{\gamma}_{,1}(x_1) = \dot{\gamma}(0) \left(\delta \left(x_1 + \frac{s}{2} \right) - \delta \left(x_1 - \frac{s}{2} \right) \right) \qquad (92)$$

The integration of these Dirac functions (in fact the absolute values due to (91)) on the interval $[-s/2, s/2 + h]$ finally gives

$$s \left(\tau^{rmC} c - \sigma_{12} \right) \dot{\gamma}(0) + 2c \, Gb\dot{\gamma}(0) = 0 \qquad (93)$$

The scaling law follows:

$$\sigma_{12} = \tau^C + \frac{2c \, Gb}{s}. \qquad (94)$$
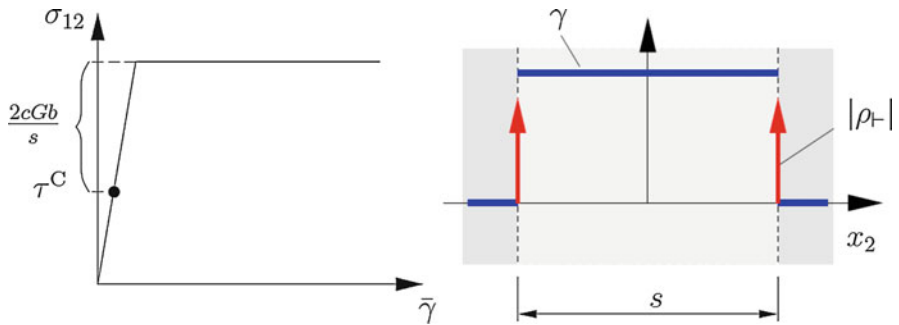
Fig. 4 Macroscopic shear stress–strain curve for the rank-one energy. The increase of the overall yield point scales inversely with the size of the soft phase, after Wulfinghoff et al. (2015)

This equation holds in the plastic regime. Clearly, the application of the rank-one energy increases the macroscopic yield stress by $2cGb/s$, i.e., the increase scales inversely with the size of the soft phase (see Fig. 4). The same scaling behavior has been found by Ohno and Okumura (2007) for a spherical grain, also using a rank-one energy. The authors concentrated on the overall mechanical response without having to compute the fields inside of the grains. As illustrated in Fig. 4, the dislocations localize in dislocation walls at the elasto-plastic interface.

For the material parameters of aluminum ($G = 26.12$ GPa and $b = 0.286$ nm) and $c = 1$, the size effect becomes important when the system size is below $10\,\mu$m. The plastic shear strain is constant in the bulk, i.e., the dislocations form singularities (walls) at the boundaries. The back stress is constant (w.r.t. space) in the bulk. During the first period, it increases and thereby impedes any plastic deformation. Therefore, the overall deformation is purely elastic during this period. At a certain point, the plastic deformation starts, and the back stress remains constant afterward. Its value is given by $2cGb/s$.

Logarithmic Energy

This section investigates the following defect energy:

$$W_{\mathrm{g}}^{\ln} = c_0 \|\mathbf{A}\| \ln \frac{\|\mathbf{A}\|}{A_0}, \tag{95}$$

with the constant c_0 as defined in Eq. (77). The energy is motivated by the statistical theory of dislocations by Groma et al. (2003). The authors derive a back stress term which involves the second gradient of slip as postulated by Aifantis (1987). However, their theory involves an internal length scale which is given by $1/\sqrt{\rho}$, where ρ denotes the total dislocation density.

In pure metals, the geometrical characteristics of the microstructure are essentially determined by the dislocation arrangement. This is a strong argument for a (variable) internal length scale, which is determined by the available dislocation

field variables (instead of a constant length scale parameter; see also Forest and Sedláček (2003b) where this dependency is derived from a dislocation line tension model).

It is demonstrated subsequently that the approach (95) leads to a back stress which is similar to that of Groma et al. (2003). However, it should be mentioned that this energy is neither convex nor smooth with respect to the dislocation density tensor (a regularization will be discussed at a later stage).

For the laminate problem, the generalized stress M reads (see Eq. (84)):

$$M = -\text{sign } \rho_\perp c_0 \left(\ln \frac{|\rho_\perp|}{A_0} + 1 \right). \tag{96}$$

In this section, rate-independent plasticity will be considered based on the yield criterion:

$$f = \left| \tau^{\text{eff}} \right| - \tau^{\text{C}} \le 0. \tag{97}$$

Here, the effective stress reads:

$$\tau^{\text{eff}} = (\boldsymbol{\sigma} + s) \cdot (\boldsymbol{l} \otimes \boldsymbol{n}) = \sigma_{12} + s_{12} \overset{(85)}{=} \sigma_{12} + M'. \tag{98}$$

With Eq. (96) and $M' = (\partial_{\rho\perp} M) \ (\partial_{x1} \rho_\perp)$, it follows that

$$\tau^{\text{eff}} = \tau - \frac{c_0}{|\rho_\perp|} \partial_{x1} \rho_\perp = \tau + \frac{G\beta}{2\pi (1-v)} \frac{b}{|\rho_\perp|} \partial_{x_1}^2 \gamma. \tag{99}$$

Here, the second term can be interpreted as a back stress. Note that the back stress involves no internal length scale parameter. Instead, the internal length scale, $\sqrt{b/\rho_\perp}$, is determined by the dislocation microstructure. In contrast to the back stress of Groma et al. (2003), the internal length scale is determined by the GND density $\rho_\perp$ instead of the total density ρ. Hence, the influence of statistically stored dislocations (SSDs) is ignored for brevity. Therefore, a homogeneous initial GND density $|\rho_\perp| = A_0$ will be assumed to be given. In addition, it is assumed that the SSD density is equal or less than A_0. The soft phase is assumed to be under plastic loading, with $\tau^{\text{eff}} = \tau^{\text{C}}$ in the soft phase. In this case,

$$M' \overset{(85)}{=} s_{12} = -\left(\sigma_{12} - \tau^{\text{C}} \right) = \text{const.} \Rightarrow M = -\left(\sigma_{12} - \tau^{\text{C}} \right) x_1, \tag{100}$$

where, again, the constant of integration vanishes due to the symmetry requirement $|M(-s/2)| = |M(s/2)|$. The plastic slip γ can be derived from the equality of Eqns. (96) and (100), which yields a differential equation for γ. The solution reads:

$$\gamma = \frac{A_0 L}{e} \left(\exp \left(\frac{s}{2L} \right) - \exp \left(-a \frac{x_1}{L} \right) \right) \text{ with } L = \frac{c_0}{\sigma_{12} - \tau^{\text{C}}}, \tag{101}$$

Fig. 5 Macroscopic
stress–strain diagram for
three different sizes.
Analytical (*lines*) and
regularized, numerical
(*triangles*) solution for the
logarithmic potential, after
Wulfinghoff et al. (2015)
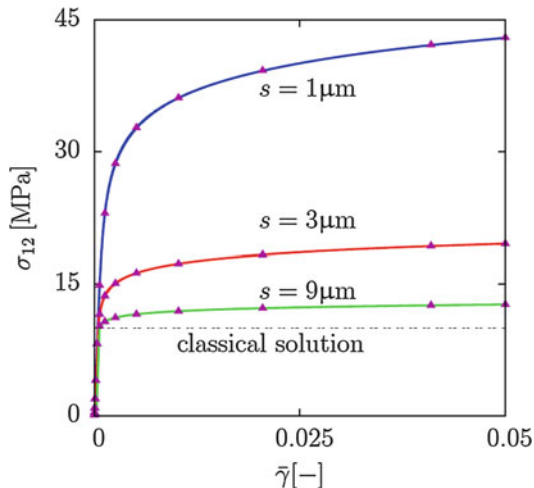
where the matching conditions $\gamma(-s/2) = \gamma(s/2) = 0$ have been exploited and where
$e = \exp(1)$. The variable a is defined by $a = \mathrm{sign}\,\gamma'$ and is assumed positive in
$(-s/2, 0)$ and negative in $(0, s/2)$.

The macroscopic stress–strain relation follows:

$$\overline{\gamma} = \frac{A_0 L}{e\,(s+h)}\left(\exp\left(\frac{s}{2L}\right)(s - 2L) + 2L\right) + \frac{\sigma_{12}}{G}. \tag{102}$$

The solution is evaluated for the following material parameters:

E [GPa]	ν	τ^C [MPa]	b [nm]	β	A_0/b [μm^{-2}]
70	0.34	10	0.286	1	1

A very thin hard phase with negligible width h is considered ($h/s = 10^{-6}$ for the
analytical solution).

The macroscopic stress–strain curve (102) is illustrated in Fig. 5. A clear
size effect is visible. Apparently, mainly the overall yield stress is affected. The
hardening shows less size dependence. It is remarkable that the model provides a
size-dependent yield stress and nonlinear kinematic hardening.

Since there is no distinct yield stress, the evaluation of the scaling behavior
is based on the offset yield stress at 0.2% plastic strain. The offset yield stress
as a function of the inverse of the size $1/s$ exhibits the same behavior as in the
results obtained from the rank-one energy. It scales inversely with channel size; see
Wulfinghoff et al. (2015).

Regularization of the Logarithmic Energy

The following regularization is introduced:

$$W_g = \begin{cases} \frac{1}{2}\frac{c_0}{b}l^2\|\mathrm{A}\|^2, & \|\mathrm{A}\| < A_{\mathrm{L}} \\ c_0\,\|\mathrm{A}\| \ln \frac{\|A\|}{A_0} + W_0, & \text{else.} \end{cases} \tag{103}$$

In the region of small GND densities, the energy is replaced by a quadratic potential. The internal length scale l, the transition density α_{L}, and the offset energy W_0 are chosen such that W_g, $\partial_{\|\alpha\|}W_g$ and $\partial^2_{\|\alpha\|}W_g$ are continuous at the transition point $\|\mathrm{A}\| = A_{\mathrm{L}}$. As a result

$$A_{\mathrm{L}} = A_0, \; l^2 = \frac{b}{A_0}, \; W_0 = \frac{c_0 A_0}{2}. \tag{104}$$

The regularized energy (103) is convex, normalized, and twice differentiable. The back stress for the laminate problem reads:

$$x = \begin{cases} -\frac{c_0}{A_0}\partial^2_{x_1}\gamma, & |\rho_\perp| < A_0, \\ -\frac{c_0}{|\rho_\perp|}\partial^2_{x_1}\gamma, & \text{else.} \end{cases} \tag{105}$$

Cyclic Behavior of the Laminate

The laminate is now submitted to one full cycle $\overline{\gamma} = \pm 0.05$. The hysteresis loops σ_{12} vs. $\overline{\gamma}$ for both rank-one and logarithmic potentials are represented in Fig. 6 for $s = 3$ µm. In the absence of isotropic hardening, the loops are stabilized after one full cycle. They are characterized by pure kinematic hardening. The influence of the back stress is clearly observable. The curves in Fig. 6 have been obtained numerically. One striking feature of the results is the nonconvexity of the obtained loops. According to the rank-one model, the first unloading stage is characterized by reverse plasticity at a constant negative shear stress. When $\overline{\gamma}$ goes through zero again, the overall shear stress experiences a jump of the same magnitude as computed analytically for monotonic loading in sections "Rank-One Defect Energy" and "Logarithmic Energy." The nonconvex loop obtained for the logarithmic potential is similar but smoother and displays smooth nonlinear kinematic hardening. A similar nonconvex hysteresis loop was obtained by Ohno and Okumura (2008) for the rank-one model.

The type of nonlinear kinematic hardening observed for both models can be identified with Asaro's type KIII model, corresponding to a *first-in/last-out* sequence of dislocation motion (Asaro (1975)). It is considered by Asaro as the most perfect form of recovery of plastic memory. Such stress–strain loops display inflection points that are observed in some materials, see Asaro (1975) for a Nimonic alloy, but such observations have also been made in several Nickel based superalloys. It is usually attributed to substructural recovery on the microscale, for instance pileup formation and destruction at γ' precipitates. In the present
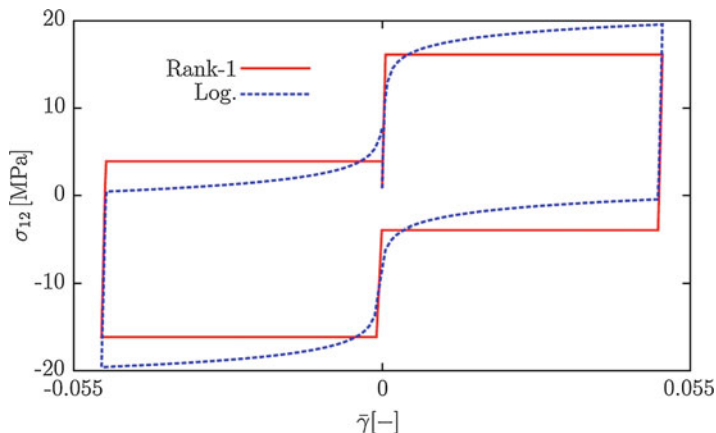
Fig. 6 Cyclic loading for s $= 3\mu$m

simple single-crystal model, it is the single active hardening mechanism induced by strain gradient plasticity and the presence of the hard phase in the laminate. It represents an accurate continuum description of dislocation piling-up and unpiling-up phenomena.

   The experimental evidence of such nonconvex loops is illustrated in Figs. 7 and 8 in the case of polycrystalline Fe–Cr and Al–Cu–Mg alloys, respectively. The first loop in Fig. 7 (left) exhibits two inflection points, but the convexity is restored after a few cycles, and the usual shape with still a strong Bauschinger effect is retrieved in Fig. 7 (right). Figure 8 shows that the amount of plastic recoverability is controlled by the annealing degree of the dislocation microstructure. Further evidence of nonconvex loops in the cyclic behavior of FCC alloys can be found in the recent contribution by Proudhon et al. (2008) dealing with aluminum alloys. The common characteristics of these FCC alloys are that they all contain a population of nonshearable intragranular precipitates. This distribution of particles represents the first series of obstacles to be overcome by dislocations for the plasticity to start. The distance between precipitates presents a small scatter, and the average value is the characteristic length responsible for the size-dependent yield limit. This distance is comparable to the width s in our ideal laminate model. As illustrated by the TEM observations by Stoltz and Pelloux (1974, 1976), Taillard and Pineau (1982), and Proudhon et al. (2008), dislocation loops multiply around precipitates and can be destroyed after reverse loading unless the material is annealed before reversing the load, see Fig. 8, or unless the multiplication of forest dislocations or cross-slip effects limit the recoverability of cyclic plasticity. The effect has also been observed in nickel-base single-crystal superalloys for tension along <111>; see Fig. 9. The simulations based on the logarithmic potential provide smooth loops that are closer to the experimental shapes. Our simulations deal with ideal single-crystal laminates and simulations for polycrystals remain to be done. However, as shown by the two-dimensional strain gradient plasticity simulations performed by Ohno and Okumura (2008), based on the rank-one potential, the effect pertains
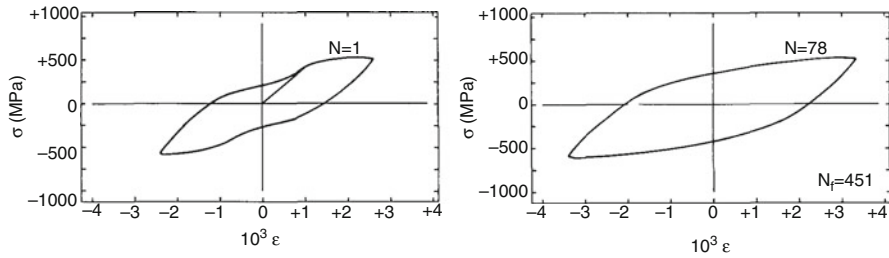
Fig. 7 Shape of the stress–strain hysteresis loop as a function of the number N of cycles for a Fe-19wt.%Cr alloy aged at 923 K for 72 h and mechanically tested at room temperature: N = 1 (left), N = 48 (right, N_f indicates the number of cycles to failure), after Taillard and Pineau (1982)
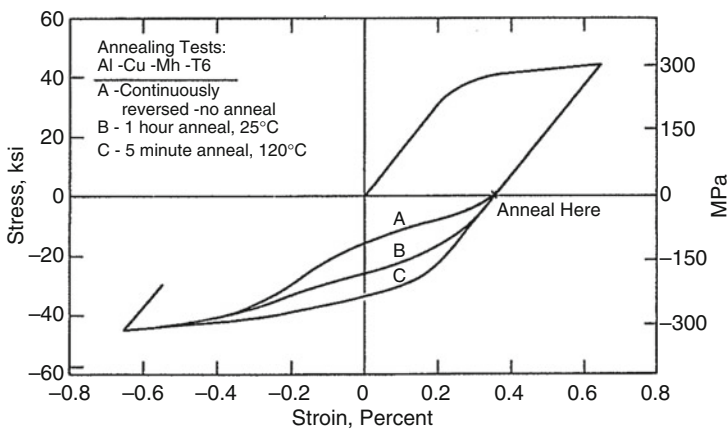
Fig. 8 Interrupted annealing hysteresis curves for an Al–Cu–Mg–T6 alloy tested at room temperature: A, continuously reverse load (no anneal); B, annealed 1 h/25 °C; and C, annealed 5 min/120 °C, after Stoltz and Pelloux (1976)

for polycrystals. However, these authors did not recognize the physical reality of the simulated phenomena. Instead, they further developed the model to replace the rank-one energy potential by a dissipative formulation which restores the convexity of fatigue loops.

The two nonquadratic energy potentials represent continuum models of a discrete phenomenon which can be illustrated for a single dislocation source, as shown in Fig. 10. The cyclic response of a Frank–Read source, simulated by discrete dislocation dynamics (DDD) (Déprés et al. 2004; Chang et al. 2016), provides a nonconvex loop which is identical to the one predicted by the rank-one continuum model. This is related to the fact that an instability of the loop behavior is observed for a critical stress that is inversely proportional to the length of the source. The scenario of dislocation source bowing and sudden propagation and multiplication can be reversed entirely in the absence of strong interaction with the dislocation forest and in the absence of cross-slip. This explains the concave shape of the stress–strain loop predicted by the DDD, which is accurately translated by the continuum
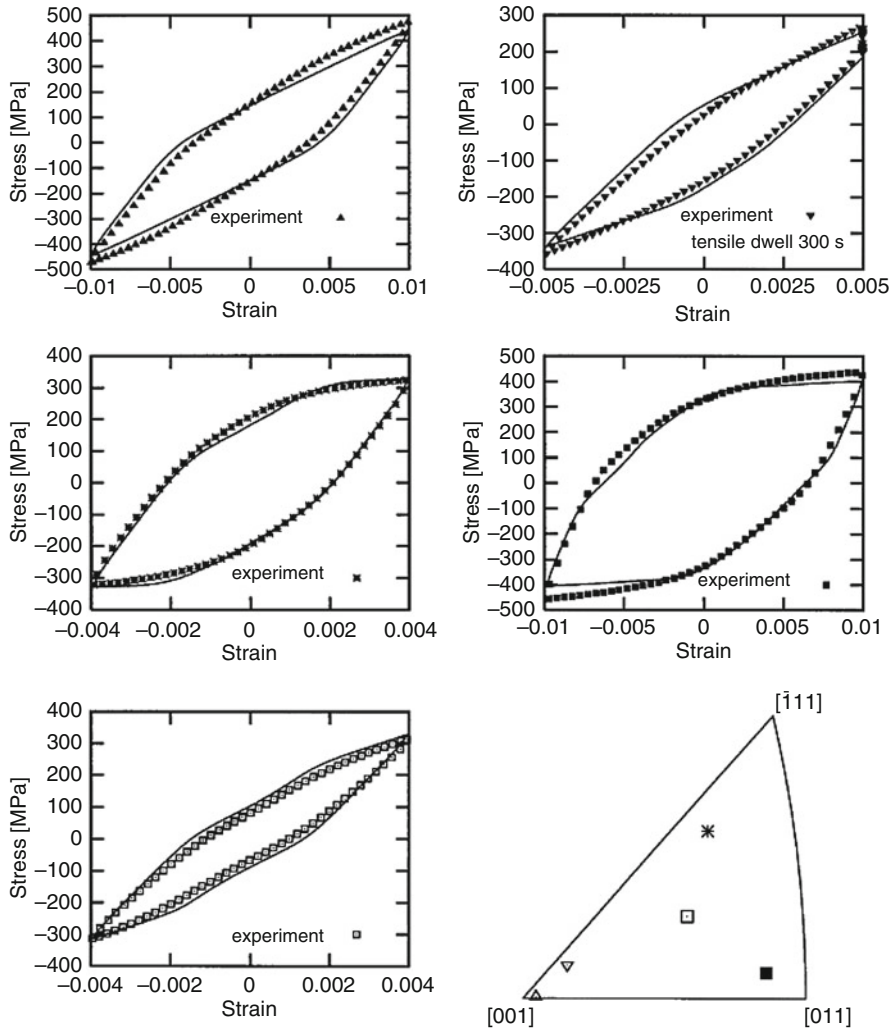
Fig. 9 Stabilized stress–strain loops for nickel-base single-crystal superalloy SC16 at 950 °C, experiment vs. simulation after Fedelich (2002)

model; see Fig. 6. Statistical effects of the collective behavior of dislocations finally destroy the recoverability of plastic deformation and the associated transmission of the single source behavior to the macroscopic response.

Grain Size Effects in Polycrystals

The model is now applied to simulate the response of polycrystals and the effects of grain size.
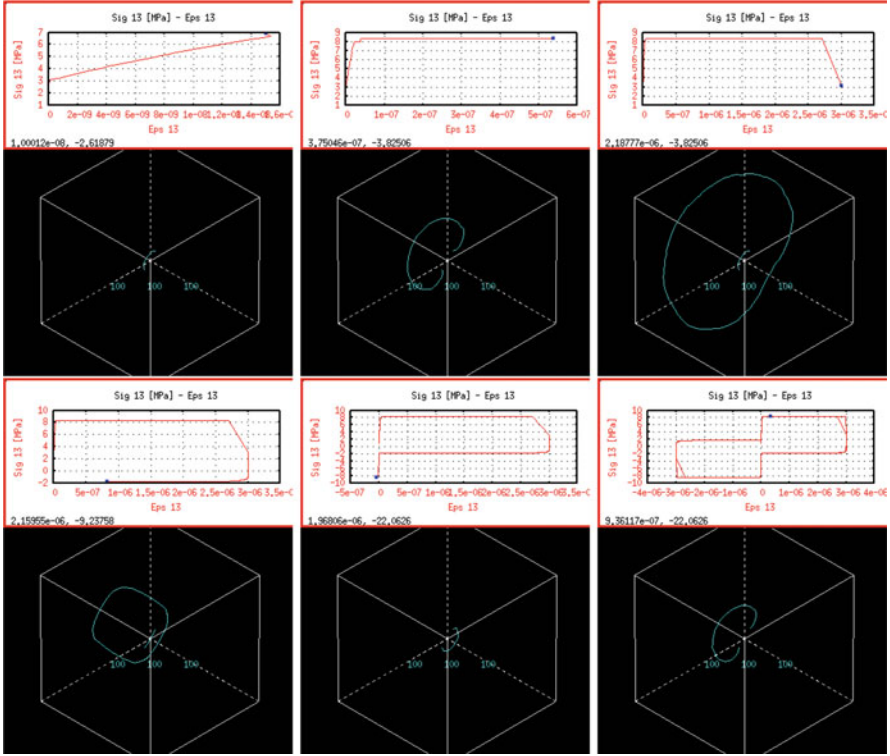
Fig. 10 Cyclic behavior of a single Frank–Read dislocation source simulated by discrete dislocation density. (Courtesy of Dr. M. Fivel)

The interface conditions at grain boundaries play a major role in the simulated size effects in the polycrystal behavior. No special interface law is considered in this work, although such physically motivated interface conditions exist in the literature; see Gurtin and Anand (2008). Instead, we consider the canonical interface conditions that arise from the formulation of the balance equations of the *microcurl* continuum model. These conditions are the continuity of displacement, u, and the continuity of plastic microdeformation, χ^p. These conditions also include the continuity of the simple and double tractions, t and $\mathbf{M}$, described in Eq. (8). Continuity of displacement excludes grain boundary cracking and sliding. Continuity of plastic microdeformation is reminiscent of the fact that dislocations generally do not cross grain boundaries, especially for such random grain boundaries. Note that in the *microcurl* model, only the kinematic degrees of freedom χ^p are continuous. This is not the case of the plastic deformation, $\mathbf{H}^p$, which is treated here as an internal variable. However, due to the internal constraint discussed in section "Model Formulation," $\mathbf{H}^p$ closely follows the plastic microdeformation so that it is quasi-continuous at grain boundaries when the penalty coefficient, H_χ, is high

enough. Conversely, lower values of H_χ may allow slightly discontinuous plastic deformation, which may be tentatively interpreted as dislocation sinking inside grain boundaries. The continuity of the associated tractions expresses the transmission of classical and generalized internal forces from one grain to another through grain boundaries. Such continuum models are then able to mimic in that way the development of dislocation pileups at grain boundaries (Forest and Sedláček 2003a).

More elaborate grain boundary behavior laws are necessary to go beyond the three possible interface conditions readily available according to the *microcurl* model: vanishing microdeformation, continuous microdeformation, or vanishing microtractions at grain boundaries. They require proper account of transmission and absorption rules for dislocations at grain boundaries. A simple and efficient strategy was proposed for the formulation and finite element implementation of such interface constitutive laws by Wulfinghoff et al. (2013a). The reader is referred to the references quoted therein for more advanced grain boundary behavior laws.

Boundary Value Problem for Polycrystals

The size effects exhibited by the solution of the boundary value problem are linked to an intrinsic length scale, l_s, introduced through the generalized moduli H_χ and A of Eq. (32) and defined as:

$$l_s = \sqrt{\frac{A}{H_\chi}}. \tag{106}$$

This intrinsic length scale has to be consistent with the fact that plasticity effects occur at scales ranging from hundreds of nanometers to a few microns. In addition, as stated in section "Model Formulation," the coupling modulus, H_χ, has to be chosen high enough to ensure that χ^p and $\mathbf{H}^p$ are close. These requirements are guidelines for the choice of relevant generalized moduli H_χ and A. The sets of material parameters used in this section are chosen in that way.

The finite element simulations have been made on periodic 2D meshes of periodic polycrystalline aggregates generated by a method based on Voronoi tessellations (Fig. 11a, b). Quadratic isoparametric finite elements with reduced integration are used. The random distribution of the grain centers has been controlled so that their sizes are sensibly the same, around the mean grain size, d. A random orientation is assigned to each grain, and two slip systems are taken into account for simplicity. In 2D, the plastic behavior of FCC crystals can be simulated with 2D planar double slip by considering two effective slip systems separated by an angle of 2ϕ (Asaro 1983; Bennett and McDowell 2003). Figure 11c describes the geometry. The slip system pair is oriented by the angle θ, which is the grain orientation randomly fixed for each grain. For a FCC crystal $\phi = 35.1°$, it corresponds to the orientation of the close-packed planes in the crystal lattice of the grain.
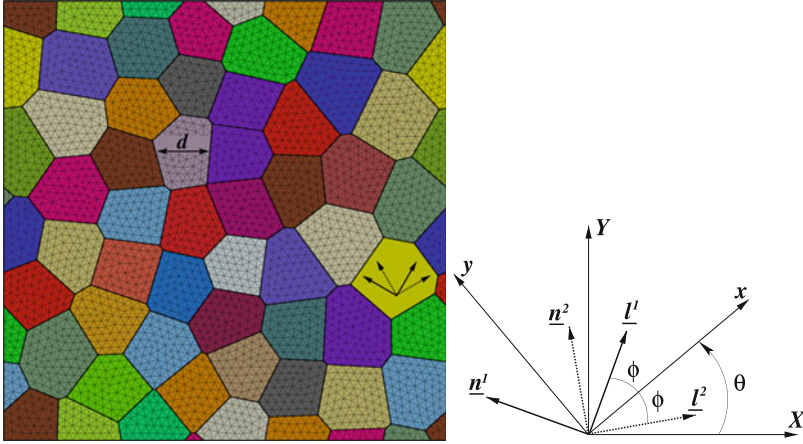
Fig. 11 Periodic meshes of the 2D periodic aggregates used in the finite element simulations including 52 grains. Two slip systems are taken into account in each randomly oriented grain. Various mean grain sizes, d, ranging from tens of nanometers to hundreds of microns, are investigated. On the right, description of the two effective slip systems for 2D planar double slip

Periodic homogenization for generalized continua is used to predict the effective response of the polycrystal. The displacement field is assumed to be of the form

$$\boldsymbol{u}(x) = \boldsymbol{E}.\boldsymbol{x} + \boldsymbol{v}(x), \tag{107}$$

with the fluctuation $\boldsymbol{v}$ periodic, meaning that it takes identical values at homologous points of the unit cell (Forest et al. 2001). The plastic microdeformation field, χ^p, is assumed to be periodic, meaning that no rotational macroscopic plastic deformation is imposed to the unit cell. Its components are equal at homologous opposite nodes. According to periodic homogenization, the simple and double tractions $\boldsymbol{t}$ and $\mathbf{m}$ are antiperiodic at homologous points of the unit cell.

Polycrystals are random materials so that the periodicity constraint may lead to a bias in the estimation of the effective properties. This boundary effect can be alleviated by considering several realizations of the microstructure and performing ensemble averaging (Zeghadi et al. 2007).

Overall Cyclic Response of a Polycrystalline Aggregate

The finite element simulations of the boundary value problem presented previously have been conducted under generalized plane strain conditions on aggregates with a relatively small number of grains. The aim here is not to obtain a representative response but to catch the grain size effects and to explore qualitatively the impact of different sets of material parameters. In this section, a virtual material is considered with various intrinsic length scales. The macroscopic stress–strain curve

Table 2 Sets of material parameters used in the 24-grain aggregate case (Fig. 11a). The intrinsic length scale, $l_s = \sqrt{A/H_\chi}$, is given for each set

Set	μ [MPa]	τ_c [MPa]	H_χ [MPa]	A [MPa mm^2]	l_s [μm]
a	35,000	40	3.0 10^6	1.0 10^{-2}	5.8 10^{-2}
b	35,000	40	1.0 10^6	1.0 10^{-2}	1.0 10^{-1}
c	35,000	40	3.5 10^5	1.0 10^{-2}	1.7 10^{-1}
d	35,000	40	8.8 10^4	1.0 10^{-3}	1.1 10^{-1}
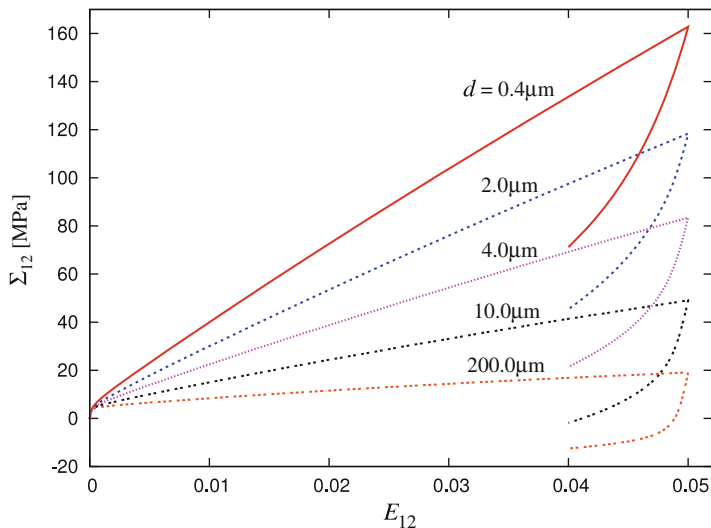
Fig. 12 Macroscopic stress–strain response of the 52-grain aggregate under simple shear for various mean grain sizes, d. The set of material parameters used is labeled (g) in Table 3

is obtained by applying a cyclic simple shear loading controlled by the average strain component E_{12} on the aggregate of 52 grains with $d = 0.2\ \mu$m and the set of material parameters labeled (c) in Table 2. The mean stress component Σ_{12} is then computed:

$$\Sigma_{12} = \frac{1}{V} \int_V \sigma_{12}\ dV, \ E_{12} = \frac{1}{V} \int_V \varepsilon_{12}\ dV, \tag{108}$$

where V denotes each polycrystal unit cell. The simulated response displays the kinematic hardening effect produced by the *microcurl* model. The stress–strain curves shown in Fig. 12 prove that this kinematic hardening is size dependent: it increases for smaller grains. Note that the observed overall kinematic hardening has two distinct sources: the intragranular back stress induced by plastic strain gradients and the intergranular internal stress that originates from the grain to grain plastic strain incompatibilities. The latter contribution is also predicted by classical crystal plasticity models.
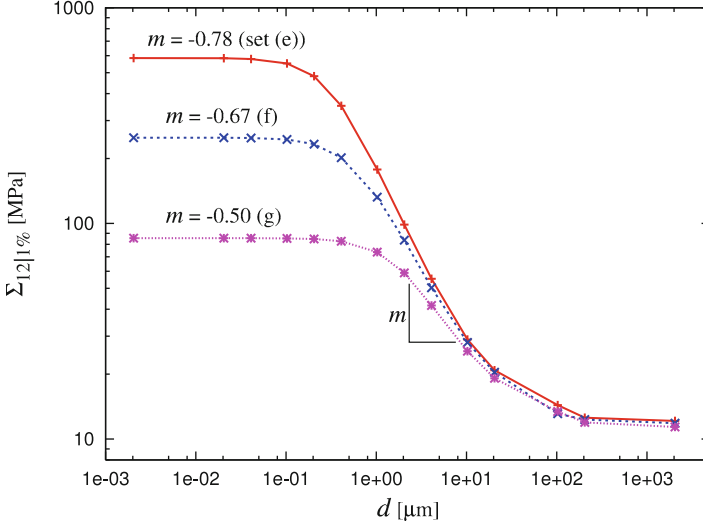
Fig. 13 Effect of the mean grain size, d, on the macroscopic flow stress, $\sum_{12|1\%}$, at 1% plastic strain. The results are obtained for the 52-grain aggregate using the different sets of material parameters given in Table 3. The scaling law exponent, m, is identified in each case

Figure 13 presents the effect of the mean grain size, d, on the macroscopic flow stress at 1% plastic strain in the 52-grain aggregate in a log–log diagram for different intrinsic length scales, l_S, introduced through the sets of material parameters (labeled a, b, c, and d) given in Table 2. The considered loading conditions are still a simple shear test with periodic boundary conditions. The curves exhibit two plateaus for large (d > 20μm) and small (d < 0.1 μm) mean grain sizes with a transition domain in between. This tanh shape indicates that when d is large compared to the intrinsic length scale, l_s, strain gradient effects are small, and the kinematic hardening arising from the *microcurl* model vanishes. The model saturates when d is of the order of l_s or smaller. The transition domain exhibits a strong size dependence, the polycrystalline aggregate becoming harder for decreasing grain sizes. The position of the transition zone, the maximum extra stress (the distance between the two plateaus), and the scaling law exponent, m, in the size-dependent domain are controlled by the material parameters used in the model. The two latter effects are controlled by the coupling modulus, H_χ; they both increase for higher values of H_χ as shown in Fig. 13. The scaling exponent is defined as the slope in the log–log diagram in the inflection domain, reflecting the scaling law:

$$\Sigma_{12} \propto d^m. \tag{109}$$

It is obtained with the sets of material parameters given in Table 2. The computed values range from -0.26 to -0.64 including the well-known Hall–Petch exponent

Table 3 Sets of material parameters used in the 52-grain aggregate case (Fig. 11b)

Set	μ [MPa]	τ_c [MPa]	Q [MPa]	b	$h^{\alpha\alpha}$	$h^{\alpha\beta, \alpha \neq \beta}$
e	27,000	0.75	7.9	10.2	1	4.4
f	27,000	0.75	7.9	10.2	1	4.4
g	27,000	0.75	7.9	10.2	1	4.4

Set	H_χ [MPa]	A [MPa mm^2]	l_s [μm]
e	$1.0\ 10^6$	$1.0\ 10^{-2}$	$1.0\ 10^{-1}$
f	$3.5\ 10^5$	$1.0\ 10^{-2}$	$1.7\ 10^{-1}$
g	$5.0\ 10^4$	$1.0\ 10^{-2}$	$4.5\ 10^{-1}$

$m = -0.5$. In fact, it was shown in Cordero et al. (2010a) that values of m ranging from 0 to -2 can be simulated with the *microcurl* model in the case of two-phase microstructures. In each case, these values are obtained without classical isotropic hardening, meaning that the linear kinematic hardening produced by the model is able to reproduce a wide range of scaling laws. Note that conventional strain gradient plasticity models do not lead to *tanh*-shape curves but rather to unbounded stress increase for vanishingly small microstructures (Cordero et al. 2010a).

Grain Size Effects in Idealized Aluminum Polycrystals

Similar finite element simulations have been performed on the idealized aluminum aggregate of 52 grains of Fig. 11. An additional isotropic hardening component is addedas in (Méric et al. 1991) to obtain a more realistic response of large aluminum grains. The size-independent hardening law reads:

$$R^\alpha = \tau_c + Q \sum_\beta^n h^{\alpha\beta} \left(1 - \exp\left(-b\gamma_{\text{cum}}^\beta\right)\right), \tag{110}$$

where n is the number of slip systems (here $n = 2$), Q and b are material coefficients defining nonlinear isotropic hardening, $H^{\alpha\beta}$ is the interaction matrix, and $\gamma_{\text{cum}}^\beta$ is the accumulated micro-plastic slip on the slip system β. Cumulative plastic slip results from the integration of the differential equation $\dot{\gamma}_{\text{cum}}^\beta = \left|\dot{\gamma}^\beta\right|$. The material parameters used in these simulations are given in Table 3. The macroscopic stress–strain curves presented in Fig. 12 are obtained by applying a simple shear loading controlled by the average strain component E_{12} on the 52-grain aggregate with various mean grain sizes, d, taken in the size-dependent domain. The chosen set of material parameters has the label (g) in Table 3. These parameters are such that an acceptable description of aluminum polycrystals is obtained for large grains and that a Hall–Petch-like behavior is found in a plausible range of grain sizes. However, we did not attempt to calibrate the amplitude of the extra hardening so that simulation predictions remain qualitative. The curves of Fig. 12 show again that the kinematic
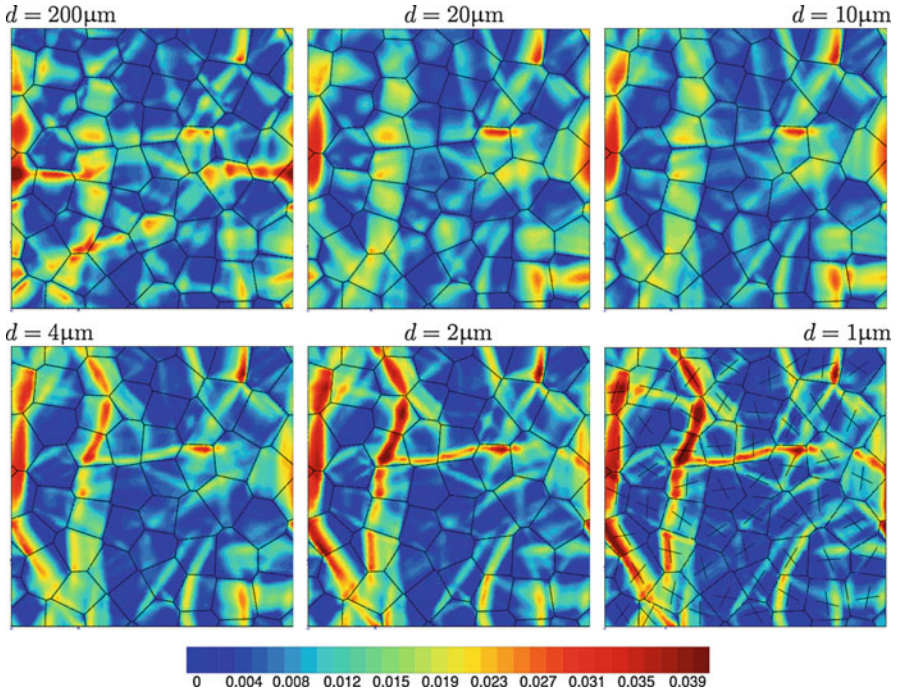
Fig. 14 Grain size effect on the accumulated plastic slip. These contour plots are obtained with the 52-grain aggregate for the same mean value of cumulative plastic strain $p = 0.01$. The set of material parameters (g) of Table 3 is used. The pairs of slip plane directions are represented for each grain on the 1 μm contour plot

hardening produced by the model is strongly size dependent. The set of material parameters (g) of Table 3 gives the ideal Hall–Petch scaling law exponent $m = -0.5$.

An important output of the simulations is the dependence of the stress and strain fields in the grains of the polycrystal on grain size. Figures 14 and 15 show the contour plots of the field of accumulated plastic slip, computed as:

$$\dot{p} = \sqrt{\frac{2}{3}\dot{\boldsymbol{\varepsilon}}^p : \dot{\boldsymbol{\varepsilon}}^p}, \tag{111}$$

where ε^p is the symmetric part of the plastic deformation, $\mathbf{H}^p$, and the contour plots of the norm $\mathbf{A}$ of the dislocation density tensor,

$$\|\mathbf{A}\| = \sqrt{\mathbf{A} : \mathbf{A}}, \tag{112}$$

respectively. The considered grain sizes are taken in the size-dependent domain where the evolution of the fields is assumed to be physically relevant. The chosen
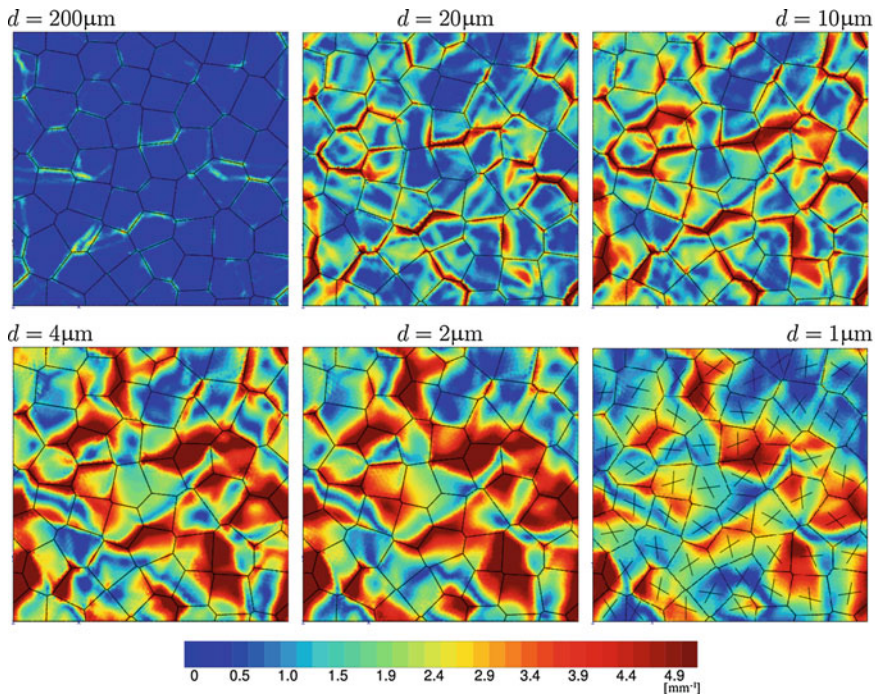
Fig. 15 Grain size effect on the norm of the dislocation density tensor. These contour plots are obtained with the 52-grain aggregate for the same mean value of macroscopic accumulated plastic strain $p = 0.01$. The set of material parameters (g) of Table 3 is used. The pairs of slip plane directions are represented for each grain on the 1 μm contour plot

set of material parameters has the label (g) in Table 3; it corresponds to an intrinsic length scale $l_s = 0.45$μm and gives a scaling law exponent $m = -0.5$. The mean value of the accumulated plastic slip is the same for all cases; only its distribution varies with the size of the microstructure as shown in Fig. 14.

The first contour plot of each figure is obtained for $d = 200$ μm $\gg l_s = 0.45$μm, at the very beginning of the size-dependent behavior domain according to Fig. 13. At this size, the simulated fields show that p is quite inhomogeneous and that some deformation bands appear; $||\mathbf{A}||$ is localized at the grain boundaries and almost vanishes in the grain cores. The contour plots obtained for 2μm $< d < 20$ μm show a significant evolution of both fields. One observes the formation of a network of strain localization bands with decreasing grain size. These bands are slip bands as they are parallel to the slip plane directions represented on the 1 μm contour plot of Fig. 14. They compensate the larger blue zones where plastic strain cannot develop due to the higher energy cost associated with its gradient. Plastic strain becomes stronger inside the localization bands. This is due to the fact that the contour plots are given for fixed macroscopic cumulative plastic strain mean value of p, which implies that the applied total strain is higher for small grain sizes as suggested by

Fig. 12. The field of the norm of the dislocation density tensor is still high close to grain boundaries and spreads over the grain cores. The last contour plot of each figure is obtained for $d = 1 \, \mu\text{m}$, a size close to l_s. Here the model starts to saturate, which can be seen from the simulated fields. The field of p does not evolve anymore and $||\mathbf{A}||$ decreases. In fact, as l_s controls the strain gradient effects, strong strain gradients cannot develop because they become energetically too expensive when the grain size is too small.

Conclusions

The micromorphic crystal plasticity theory introduces independent plastic microdeformation degrees of freedom. It represents a relaxation of the strain gradient plasticity model. It contains as a special case the micropolar crystal plasticity model. The advantage of the micromorphic framework is that it provides a wider range of modeling possibilities regarding constitutive laws and boundary conditions, as it was illustrated for the description of Hall–Petch effects in polycrystals. It has also merits regarding computational mechanical aspects since its implementation is rather straightforward and can be used for strain gradient plasticity computations based on proper internal constraints. The advantage of the micropolar theory compared to the micromorphic one is its reduced number of degrees of freedom, 3 instead of 8/9 in 3D (8 dof if plastic incompressibility is enforced). The micropolar model incorporates the effect of the lattice curvature tensor, which represents an essential part of the dislocation density tensor.

A full set of constitutive equations has been formulated for micromorphic crystal plasticity by extending the framework of generalized standard materials based on the introduction of free energy and dissipation potentials.

Simple examples of the plasticity of sheared single-crystal layers show the ability of the continuum models to reproduce the essential features of the collective behavior of dislocations piling up in thin layers, channels, and laminate microstructures, as predicted by discrete dislocation dynamics. The scaling laws predicted by the continuum models strongly depend on the choice of the constitutive equations. For example, standard quadratic free energy potential was shown to be inadequate to reproduce Orowan-like size effects. Strongly nonlinear potentials, including the logarithmic free energy density, were shown to be more closely related to the physics of dislocations.

Size effects also strongly influence the strain localization behavior of polycrystals for which the formation of intense slip bands is predicted in micron-size grains by the micromorphic models. This feature is to be related to the high energy cost of dislocation pileup formation in small grains.

Special attention was given to the cyclic response of crystals, which is of the utmost importance for the prediction of fatigue lifetime of materials. The question of recovery of plastic strain has been shown to be a central issue. In the absence of strong forest interaction and cross-slip, total recovery of plastic strain gradients is possible, leading to nonconvex cyclic stress–strain loops as observed in some

two-phase alloys. Note that results from discrete dislocation dynamics and the micropolar model were provided in the chapter dedicated to micropolar crystal plasticity. Similar comparisons can be found in the case of micromorphic model in the Reference Chang et al. (2016) where the continuum and discrete descriptions of dislocation pileups at interfaces are discussed.

Much work remains to be done in the development of predictive constitutive equations in micropolar and micromorphic crystal plasticity due to the complex underlying dislocation mechanisms. Especially, suitable modeling of grain boundary behavior remains a major issue for higher-order modeling of polycrystal plasticity.

References

E. Aifantis, The physics of plastic deformation. Int. J. Plast. **3**, 211–248 (1987)

R.J. Asaro, Elastic–plastic memory and kinematic hardening. Acta Metall. **23**, 1255–1265 (1975)

R. Asaro, Crystal plasticity. J. Appl. Mech. **50**, 921–934 (1983)

Ashby, M., 1971. The deformation of plastically non-homogeneous alloys, in *Strengthening Methods in Crystals*, ed. by A. Kelly, R. Nicholson (Applied Science Publishers, London), pp. 137–192

O. Aslan, N.M. Cordero, A. Gaubert, S. Forest, Micromorphic approach to single crystal plasticity and damage. Int. J. Eng. Sci. **49**, 1311–1325 (2011)

V. Bennett, D. McDowell, Crack tip displacements of microstructurally small surface cracks in single phase ductile polycrystals. Eng. Fract. Mech. **70**(2), 185–207 (2003)

V. Berdichevsky, On thermodynamics of crystal plasticity. Scripta Mat. **54**, 711–716 (2006a)

V. Berdichevsky, On thermodynamics of crystal plasticity. Scr. Mater. **54**, 711–716 (2006b)

P. Cermelli, M. Gurtin, On the characterization of geometrically necessary dislocations in finite plasticity. J. Mech. Phys. Solids **49**, 1539–1568 (2001)

H.J. Chang, N.M. Cordero, C. Déprés, M. Fivel, S. Forest, Micromorphic crystal plasticity versus discrete dislocation dynamics analysis of multilayer pile-up hardening in a narrow channel. Arch. Appl. Mech. **86**, 21–38 (2016)

W. Claus, A. Eringen, Three dislocation concepts and micromorphic mechanics, in *Developments in Mechanics. Proceedings of the 12th Midwestern Mechanics Conference*, vol. 6, (1969), pp. 349–358

S. Conti, M. Ortiz, Dislocation microstructures and the effective behavior of single crystals. Arch. Ration. Mech. Anal. **176**, 103–147 (2005)

N. Cordero, A. Gaubert, S. Forest, E. Busso, F. Gallerneau, S. Kruch, Size effects in generalised continuum crystal plasticity for two–phase laminates. J. Mech. Phys. Solids **58**, 1963–1994 (2010a)

N.M. Cordero, A. Gaubert, S. Forest, E. Busso, F. Gallerneau, S. Kruch, Size effects in generalised continuum crystal plasticity for two-phase laminates. J. Mech. Phys. Solids **58**, 1963–1994 (2010b)

N.M. Cordero, S. Forest, E. Busso, S. Berbenni, M. Cherkaoui, Grain size effects on plastic strain and dislocation density tensor fields in metal polycrystals. Comput. Mater. Sci. **52**, 7–13 (2012)

L. De Luca, A. Garroni, M. Ponsiglione, Gamma-convergence analysis of Systems of Edge Dislocations: the self energy regime. Arch. Ration. Mech. Anal. **206**, 885–910 (2012)

C. Déprés, C.F. Robertson, M.C. Fivel, Low-strain fatigue in aisi 316l steel surface grains: a three-dimensional discrete dislocation dynamics modelling of the early cycles i. Dislocation microstructures and mechanical behaviour. Philos. Mag. **84**(22), 2257–2275 (2004)

Eringen, A., Claus, W., 1970. A micromorphic approach to dislocation theory and its relation to several existing theories, in *Fundamental Aspects of Dislocation Theory*, ed. by J. Simmons, R. de Wit, R. Bullough. National Bureau of Standards (US) Special Publication 317, vol. II (U.S. Government Printing Office, Washington, DC), pp. 1023–1062

B. Fedelich, A microstructural model for the monotonic and the cyclic mechanical behavior of single crystals of superalloys at high temperatures. Int. J. Mech. Sci. **18**, 1–49 (2002)

S. Forest, Some links between cosserat, strain gradient crystal plasticity and the statistical theory of dislocations. Philos. Mag. **88**, 3549–3563 (2008)

S. Forest, The micromorphic approach for gradient elasticity, viscoplasticity and damage. ASCE J. Eng. Mech. **135**, 117–131 (2009)

S. Forest, Nonlinear regularisation operators as derived from the micromorphic approach to gradient elasticity, viscoplasticity and damage. Proc. R. Soc. A **472**, 20150755 (2016)

S. Forest, N. Guéninchault, Inspection of free energy functions in gradient crystal plasticity. Acta. Mech. Sinica. **29**, 763–772 (2013) https://doi.org/10.1007/s10409-013-0088-0

S. Forest, R. Sedláček, Plastic slip distribution in two–phase laminate microstructures: Dislocation–based vs. generalized–continuum approaches. Philos. Mag. A **83**, 245–276 (2003a)

S. Forest, R. Sedláček, Plastic slip distribution in two–phase laminate microstructures: Dislocation–based vs. generalized–continuum approaches. Philos. Mag. A **83**, 245–276 (2003b)

S. Forest, R. Sievert, Elastoviscoplastic constitutive frameworks for generalized continua. Acta Mech. **160**, 71–111 (2003)

S. Forest, R. Sievert, Nonlinear microstrain theories. Int. J. Solids Struct. **43**, 7224–7245 (2006)

S. Forest, F. Pradel, K. Sab, Asymptotic analysis of heterogeneous Cosserat media. Int. J. Solids Struct. **38**, 4585–4608 (2001)

Forest, S., Ammar, K., Appolaire, B., Cordero, N., Gaubert, A., 2014. Micromorphic approach to crystal plasticity and phase transformation, in *Plasticity and Beyond*, ed. by J. Schroeder, K. Hackl. CISM International Centre for Mechanical Sciences, Courses and Lectures, no. 550 (Springer, Vienna), pp. 131–198

M. Geers, R. Peerlings, M. Peletier, L. Scardia, Asymptotic behaviour of a pile–up of infinite walls of edge dislocations. Arch. Ration. Mech. Anal. **209**, 495–539 (2013)

P. Germain, The method of virtual power in continuum mechanics. Part 2: microstructure. SIAM J. Appl. Math. **25**, 556–575 (1973)

P. Grammenoudis, C. Tsakmakis, Micromorphic continuum part I: strain and stress tensors and their associated rates. Int. J. Non–Linear Mech. **44**, 943–956 (2009)

I. Groma, F. Csikor, M. Zaiser, Spatial correlations and higher–order gradient terms in a continuum description of dislocation dynamics. Acta Mater. **51**, 1271–1281 (2003)

I. Groma, G. Györgyi, B. Kocsis, Dynamics of coarse grain grained dislocation densities from an effective free energy. Philos. Mag. **87**, 1185–1199 (2007)

M. Gurtin, A gradient theory of single–crystal viscoplasticity that accounts for geometrically necessary dislocations. J. Mech. Phys. Solids **50**, 5–32 (2002)

M. Gurtin, L. Anand, Nanocrystalline grain boundaries that slip and separate: a gradient theory that accounts for grain-boundary stress and conditions at a triple-junction. J. Mech. Phys. Solids **56**, 184–199 (2008)

M. Gurtin, L. Anand, Thermodynamics applied to gradient theories involving the accumulated plastic strain: the theories of Aifantis and Fleck and Hutchinson and their generalization. J. Mech. Phys. Solids **57**, 405–421 (2009)

W. Han, B. Reddy, *Plasticity: Mathematical Theory and Numerical Analysis* (Springer, New York, 2013)

C. Hirschberger, P. Steinmann, Classification of concepts in thermodynamically consistent generalized plasticity. ASCE J. Eng.Mech. **135**, 156–170 (2009)

D.E. Hurtado, M. Ortiz, Surface effects and the size-dependent hardening and strengthening of nickel micropillars. J. Mech. Phys. Solids **60**(8), 1432–1446 (2012)

D.E. Hurtado, M. Ortiz, Finite element analysis of geometrically necessary dislocations in crystal plasticity. Int. J. Numer. Methods Eng. **93**(1), 66–79 (2013)

R. Kametani, K. Kodera, D. Okumura, N. Ohno, Implicit iterative finite element scheme for a strain gradient crystal plasticity model based on self-energy of geometrically necessary dislocations. Comput. Mater. Sci. **53**(1), 53–59 (2012)

Kröner, E., 1969. Initial studies of a plasticity theory based upon statistical mechanics, in *Inelastic Behaviour of Solids*, ed. by M. Kanninen, W. Adler, A. Rosenfield, R. Jaffee (McGraw-Hill, New York/London), pp. 137–147

J. Lee, Y. Chen, Constitutive relations of micromorphic thermoplasticity. Int. J. Eng. Sci. **41**, 387–399 (2003)

J. Mandel, Equations constitutives et directeurs dans les milieux plastiques et viscoplastiques. Int. J. Solids Struct. **9**, 725–740 (1973)

L. Méric, P. Poubanne, G. Cailletaud, Single crystal modeling for structural calculations. Part 1: Model presentation. J. Eng. Mat. Technol. **113**, 162–170 (1991)

S.D. Mesarovic, R. Baskaran, A. Panchenko, Thermodynamic coarsening of dislocation mechanics and the size-dependent continuum crystal plasticity. J. Mech. Phys. Solids **58**(3), 311–329 (2010)

S. Mesarovic, S. Forest, J. Jaric, Size-dependent energy in crystal plasticity and continuum dislocation models. Proc. R. Soc. A **471**, 20140868 (2015)

C. Miehe, S. Mauthe, F.E. Hildebrand, Variational gradient plasticity at finite strains. Part III: local-global updates and regularization techniques in multiplicative plasticity for single crystals. Comput. Methods Appl. Mech. Eng. **268**, 735–762 (2014)

J. Nye, Some geometrical relations in dislocated crystals. Acta Metall. **1**, 153–162 (1953)

N. Ohno, D. Okumura, Higher-order stress and grain size effects due to self-energy of geometrically necessary dislocations. J. Mech. Phys. Solids **55**, 1879–1898 (2007)

N. Ohno, D. Okumura, Grain–size dependent yield behavior under loading, unloading and reverse loading. Int. J. Mod. Phys. B **22**, 5937–5942 (2008)

M. Ortiz, E. Repetto, Nonconvex energy minimization and dislocation structures in ductile single crystals. J. Mech. Phys. Solids **47**(2), 397–462 (1999)

H. Proudhon, W. Poole, X. Wang, Y. Bréchet, The role of internal stresses on the plastic deformation of the Al–Mg–Si–Cu alloy AA611. Philos. Mag. **88**, 621–640 (2008)

B.D. Reddy, C. Wieners, B. Wohlmuth, Finite element analysis and algorithms for single-crystal strain-gradient plasticity. Int. J. Numer. Methods Eng. **90**(6), 784–804 (2012)

R. Regueiro, On finite strain micromorphic elastoplasticity. Int. J. Solids Struct. **47**, 786–800 (2010)

C. Sansour, S. Skatulla, H. Zbib, A formulation for the micromorphic continuum at finite inelastic strains. Int. J. Solids Struct. **47**, 1546–1554 (2010)

P. Steinmann, Views on multiplicative elastoplasticity and the continuum theory of dislocations. Int. J. Eng. Sci. **34**, 1717–1735 (1996)

R. Stoltz, R. Pelloux, Cyclic deformation and Bauschinger effect in Al–Cu–Mg alloys. Scr. Metall. **8**, 269–276 (1974)

R. Stoltz, R. Pelloux, The Bauschinger effect in precipitation strengthened aluminum alloys. Metallurgical. Transactions **7A**, 1295–1306 (1976)

B. Svendsen, S. Bargmann, On the continuum thermodynamic rate variational formulation of models for extended crystal plasticity at large deformation. J. Mech. Phys. Solids **58**(9), 1253–1271 (2010)

R. Taillard, A. Pineau, Room temperature tensile properties of Fe-19wt.% Cr alloys precipitation hardened by the intermetallic compound NiAl. Mater. Sci. Eng. **56**, 219–231 (1982)

S. Wulfinghoff, T. Böhlke, Equivalent plastic strain gradient enhancement of single crystal plasticity: theory and numerics. Proc. R. Soc. A: Math. Phys. Eng. Sci. **468**(2145), 2682–2703 (2012)

S. Wulfinghoff, E. Bayerschen, T. Böhlke, A gradient plasticity grain boundary yield theory. Int. J. Plast. **51**, 33–46 (2013a)

S. Wulfinghoff, E. Bayerschen, T. Böhlke, Micromechanical simulation of the hall-petch effect with a crystal gradient theory including a grain boundary yield criterion. PAMM **13**, 15–18 (2013b)

S. Wulfinghoff, S. Forest, T. Böhlke, Strain gradient plasticity modeling of the cyclic behavior of laminate microstructures. J. Mech. Phys. Solids **79**, 1–20 (2015)

A. Zeghadi, S. Forest, A.-F. Gourgues, O. Bouaziz, Ensemble averaging stress–strain fields in polycrystalline aggregates with a constrained surface microstructure–part 2: crystal plasticity. Philos. Mag. **87**, 1425–1446 (2007)